nature climate change

ARTICLES

https://doi.org/10.1038/s41558-020-0784-2

Check for updates

Sea-ice loss amplifies summertime decadal CO_2 increase in the western Arctic Ocean

Zhangxian Ouyang[1], Di Qi[2], Liqi Chen[2], Taro Takahashi[3,10], Wenli Zhong[4], Michael D. DeGrandpre[5], Baoshan Chen[1], Zhongyong Gao[2], Shigeto Nishino[6], Akihiko Murata[6,7], Heng Sun[2], Lisa L. Robbins[8], Meibing Jin[9] and Wei-Jun Cai[1]✉

Rapid climate warming and sea-ice loss have induced major changes in the sea surface partial pressure of CO_2 (p_{CO_2}). However, the long-term trends in the western Arctic Ocean are unknown. Here we show that in 1994–2017, summer p_{CO_2} in the Canada Basin increased at twice the rate of atmospheric increase. Warming and ice loss in the basin have strengthened the p_{CO_2} seasonal amplitude, resulting in the rapid decadal increase. Consequently, the summer air–sea CO_2 gradient has reduced rapidly, and may become near zero within two decades. In contrast, there was no significant p_{CO_2} increase on the Chukchi Shelf, where strong and increasing biological uptake has held p_{CO_2} low, and thus the CO_2 sink has increased and may increase further due to the atmospheric CO_2 increase. Our findings elucidate the contrasting physical and biological drivers controlling sea surface p_{CO_2} variations and trends in response to climate change in the Arctic Ocean.

As a bellwether of climate change, the Arctic Ocean has experienced dramatic physical and ecological changes, including warming and increased sea-ice loss[1,2], freshened surface water[3,4], altered surface circulation[5–7] and enhanced primary production[8]. These changes also influence Arctic Ocean carbonate chemistry by decreasing the carbonate mineral saturation state[9] and expanding the acidified water volume[10–12]. While sea-ice melt removes the mechanical barrier for air–sea CO_2 exchange, melt water increases the surface stratification and suppresses nutrients supplied by the upward mixing of subsurface waters[13,14], thus potentially limiting the biological drawdown of CO_2 and ocean CO_2 uptake[15].

The direction and magnitude of CO_2 uptake or release across the sea surface are determined by the air–sea difference in the partial pressure of CO_2 (p_{CO_2}). On a decadal scale, the sea surface p_{CO_2} has increased almost everywhere in the world's oceans (including the low and mid-latitudes and the Southern Ocean) at rates roughly comparable to that of the atmospheric CO_2 increase[16–18]. The trends of p_{CO_2} in the Arctic Ocean are poorly known, however, due to observational limitations and the added complexity involving sea-ice melt. Early observations suggested a strong CO_2 sink with persistently low p_{CO_2} in the highly productive shelf and slope areas[19], while more recent observations from the ice-free basin found high p_{CO_2} values approaching atmospheric CO_2 levels due to rapid air–sea gas exchange and warming[15,20]. Since these initial assessments, much more sea surface p_{CO_2} data have been collected, making it possible for the first time to identify the observation-based decadal trends and explore the driving mechanisms. Here we report new sea surface p_{CO_2} data together with historical data from multiple international databases (Supplementary Table 1) from 1994 to 2017, examine the seasonal and decadal variations, and quantify the contributions of multiple drivers. This study improves the understanding of processes regulating seasonal and interannual variabilities of the Arctic Ocean p_{CO_2}, which is essential for forecasting responses of the ocean carbon cycle to climate change.

Spatial distribution and decadal trends of sea surface p_{CO_2}

During the summer (1 July to 15 October) over the past two decades, a distinct spatial distribution of low p_{CO_2} in the surface waters of shelf areas and high p_{CO_2} in the central basins gradually formed and persistently appeared in the western Arctic Ocean (Fig. 1 and Extended Data Fig. 1). In the mid-1990s, most of the region was covered by sea ice, and p_{CO_2} showed low values on the shelf and near the ice edge (70–74° N) and higher values in more northerly ice-covered regions (Extended Data Fig. 1a). As sea ice retreated poleward in the early 2000s, moderately high p_{CO_2} appeared in the southern Canada Basin (Extended Data Fig. 1b–d). Since 2008, the central Canada Basin became more frequently ice free and exhibited conspicuously higher p_{CO_2} (Extended Data Fig. 1e–i). In more recent years, the near-atmospheric (>370 µatm) p_{CO_2} values have extended farther north into the northern basins (Extended Data Fig. 1j–l). In contrast, p_{CO_2} on the Chukchi Shelf was equally low or even lower in recent years compared with the 1990s and early 2000s, although some high p_{CO_2} signals were observed in the shallow nearshore areas (Extended Data Fig. 1). This increasingly contrasting spatial distribution of sea surface p_{CO_2} has become a new normal during summertime in the western Arctic Ocean since 2007 (Fig. 1 and Extended Data Fig. 1).

Because of the observed spatial heterogeneity, we examined the long-term rate of p_{CO_2} change separately for the Chukchi Shelf,

[1]School of Marine Science and Policy, University of Delaware, Newark, DE, USA. [2]Key Laboratory of Global Change and Marine-Atmospheric Chemistry of Ministry of Natural Resources (MNR), Third Institute of Oceanography, MNR, Xiamen, China. [3]Lamont-Doherty Earth Observatory of Columbia University, Palisades, NY, USA. [4]Key Laboratory of Physical Oceanography, Ocean University of China, Qingdao, China. [5]Department of Chemistry and Biochemistry, University of Montana, Missoula, MT, USA. [6]Institute of Arctic Climate and Environment Research, Japan Agency for Marine-Earth Science and Technology, Yokosuka, Japan. [7]Research Institute for Global Change, Japan Agency for Marine-Earth Science and Technology, Yokosuka, Japan. [8]College of Marine Science, University of South Florida, St. Petersburg, FL, USA. [9]International Arctic Research Center, Fairbanks, AK, USA. [10]Deceased: T. Takahashi. ✉e-mail: wcai@udel.edu

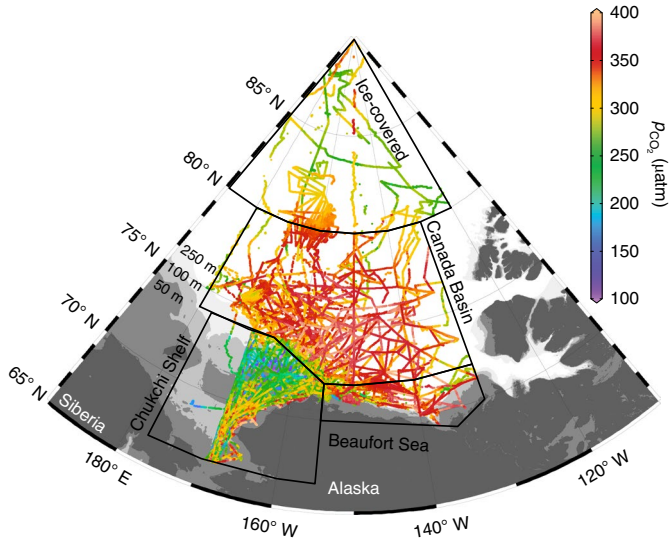

Fig. 1 | The spatial distribution of sea surface p_{CO_2}. Map of the western Arctic Ocean overlaid with p_{CO_2} observations in the summer (1 July–15 October) from 1994 to 2017. Information about the individual cruises is presented in Extended Data Fig. 1 and Supplementary Table 1. The western Arctic Ocean (<80° N) is defined as the combination of three subregions: the Chukchi Shelf, the Beaufort Sea and the Canada Basin. On the basis of the spatial heterogeneity of observed p_{CO_2}, we separate the Chukchi Shelf and the Canada Basin mainly along 200–250 m isobaths. We set the boundary for the Chukchi Shelf and the coastal Beaufort Sea at 155° W, where the Alaska coastal current loses its major impact and the Mackenzie River runoff occupies the surface water. Data for the Canada Basin and the Beaufort Sea are assigned to be north and south of 72° N, respectively. Data observed north of 80° N are assigned to the perennially ice-covered region (ice concentration >15%).

the Beaufort Sea and the mostly ice-free Canada Basin (south of 80° N), as well as the mostly ice-covered high latitudes (north of 80° N) (Fig. 1). We first investigated the temporal and spatial coverages of the observed p_{CO_2} data (Extended Data Fig. 2) as well as the possible change in p_{CO_2} seasonality (Extended Data Fig. 3), and we then examined the different timescales (daily, monthly and entire summer) and different grid sizes used for deriving the mean values to estimate the long-term trends (Supplementary Table 2). Through careful comparisons between deseasonalized and non-deseasonalized analyses (Extended Data Fig. 3) and sensitivity tests, such as randomly removing 15% or 30% of the cruises or measurements (Supplementary Figs. 1 and 2), we chose to use non-deseasonalized measurements to derive gridded (0.1° latitude × 0.25° longitude) monthly p_{CO_2} for each subregion and then conducted linear regressions for the long-term trends (Methods).

We find that sea surface p_{CO_2} increased substantially in the nearly ice-free Canada Basin south of 80° N at a rate of 4.6 ± 0.5 μatm yr^{-1} (Fig. 2a), which is much faster than in any other ocean basin[16–18] and more than two times the rate of atmospheric CO_2 increase (1.9 ± 0.1 μatm yr^{-1}). As a result, the summer averaged air–sea CO_2 gradient (Δp_{CO_2}) reduced from −100 to −50 μatm over the past two decades (Fig. 2a and Extended Data Fig. 4). If this trend continues, the Δp_{CO_2} in the ice-free basin will shrink to near 0 μatm in the 2030s, suggesting that the surface water in the basin will not be as large a CO_2 sink as previously predicted[19]. In contrast, on the Chukchi Shelf, sea surface p_{CO_2} does not exhibit a statistically significant long-term trend (Fig. 2b). Therefore, air-sea CO_2 gradient has likely increased with time. In the adjacent Beaufort Sea, the p_{CO_2} increased at a slightly lower rate than that in the Canada Basin (Fig. 2c). For most of the perennially ice-covered areas in the western Arctic Ocean north of 80° N, p_{CO_2} increased at a rate of only 1.8 ± 1.1 μatm yr^{-1}, which is statistically comparable to the rate of atmospheric CO_2 increase (Fig. 2d).

Pacific water influence and control mechanisms

The contrasting long-term trends between the Chukchi Shelf and Canada Basin indicate different mechanisms controlling the spatial and temporal variations in the surface p_{CO_2} and air–sea CO_2 flux. For the western Arctic Ocean, one notable change over the past few decades is that the annual Bering Strait throughflow has increased[21,22], bringing more nutrients onto the Chukchi Shelf and enhancing primary production[8,23]. The inflow of this nutrient-rich Pacific summer water, which is slowed down in the areas south of the Chukchi shelfbreak with a residence time of ~90 days[7], facilitates high biological productivity and the persistence of low p_{CO_2} and a large ocean CO_2 sink on the central and northern Chukchi Shelf[24].

As the Pacific water flows poleward over the shelfbreak into the Canada Basin, most of it subducts into the subsurface regime[5,25] because its density is greater than that of the surface waters in the southern Canada Basin and the Beaufort Sea slope (Fig. 3). This mechanism accounts for the observed dramatic transition from low p_{CO_2} on the shelf to high p_{CO_2} in the surface waters of the basin and slope within a very narrow front along the shelfbreak (over 200–250 m isobath, 72–74° N, Fig. 1 and Extended Data Fig. 1). This transition could be intensified by the strengthened summer easterly winds and currents, which favour east–west flows rather than flows across the shelfbreak[6,26]. However, accelerated sea-ice loss leads to a larger ice-free area in the Canada Basin. As the barrier to air–sea CO_2 exchange has been removed, the atmospheric CO_2 could rapidly invade surface water and, because of the lack of vertical mixing, push sea surface p_{CO_2} towards the atmospheric level within about two months[15,20] (Fig. 3b). This process substantially reduces the air–sea CO_2 gradient and acts as a new sea-surface barrier, inhibiting further CO_2 uptake later in the season. In addition, the spin-up of anticyclonic flow in the Beaufort Gyre in the past two decades has resulted in a fresher and shallower surface mixed layer in the Canada Basin[3,27]. In turn, the accumulation of freshwater strengthens the stratification at the base of the surface mixed layer and minimizes vertical mixing. As a consequence, the nutrient-enriched subsurface water from the Chukchi Shelf cannot play a direct role in reducing the basin surface p_{CO_2} (refs. [13,14]) (Fig. 3). Note that the Beaufort Sea does not receive abundant nutrients from the Pacific water; rather, its nutrients mostly come from the Mackenzie River and upwelled waters from the basin subsurface[28]. Its long-term variation in sea surface p_{CO_2} is therefore different from that in the Chukchi Shelf and is more like that found in the Canada Basin, except with larger seasonal and interannual variability (Fig. 2 and Extended Data Fig. 3).

Drivers and contributions to p_{CO_2} increase

To quantitatively evaluate how sea surface p_{CO_2} on the shelf and basin respond differently to environmental changes, we focused on the analysis of sea surface p_{CO_2} in the two most contrasting subregions: the Chukchi Shelf and the Canada Basin. We started with a separation of the observed sea surface p_{CO_2} change into its thermal and non-thermal components, with the former driven by the long-term change in sea surface temperature (SST), and the latter driven by the long-term variations in all other factors including dissolved inorganic carbon (DIC), total alkalinity (Alk) and a freshwater term measured by salinity change, following a well-established method[29–32] (Methods). This separation showed that the thermal component induces a substantial increase in the rates of change in sea surface p_{CO_2} in the Chukchi Shelf (1.3 ± 0.6 μatm yr^{-1}) and a moderate increase in the Canada Basin (0.6 ± 0.3 μatm yr^{-1}) (Table 1). Conversely, the non-thermal component of p_{CO_2} leads to a substan-

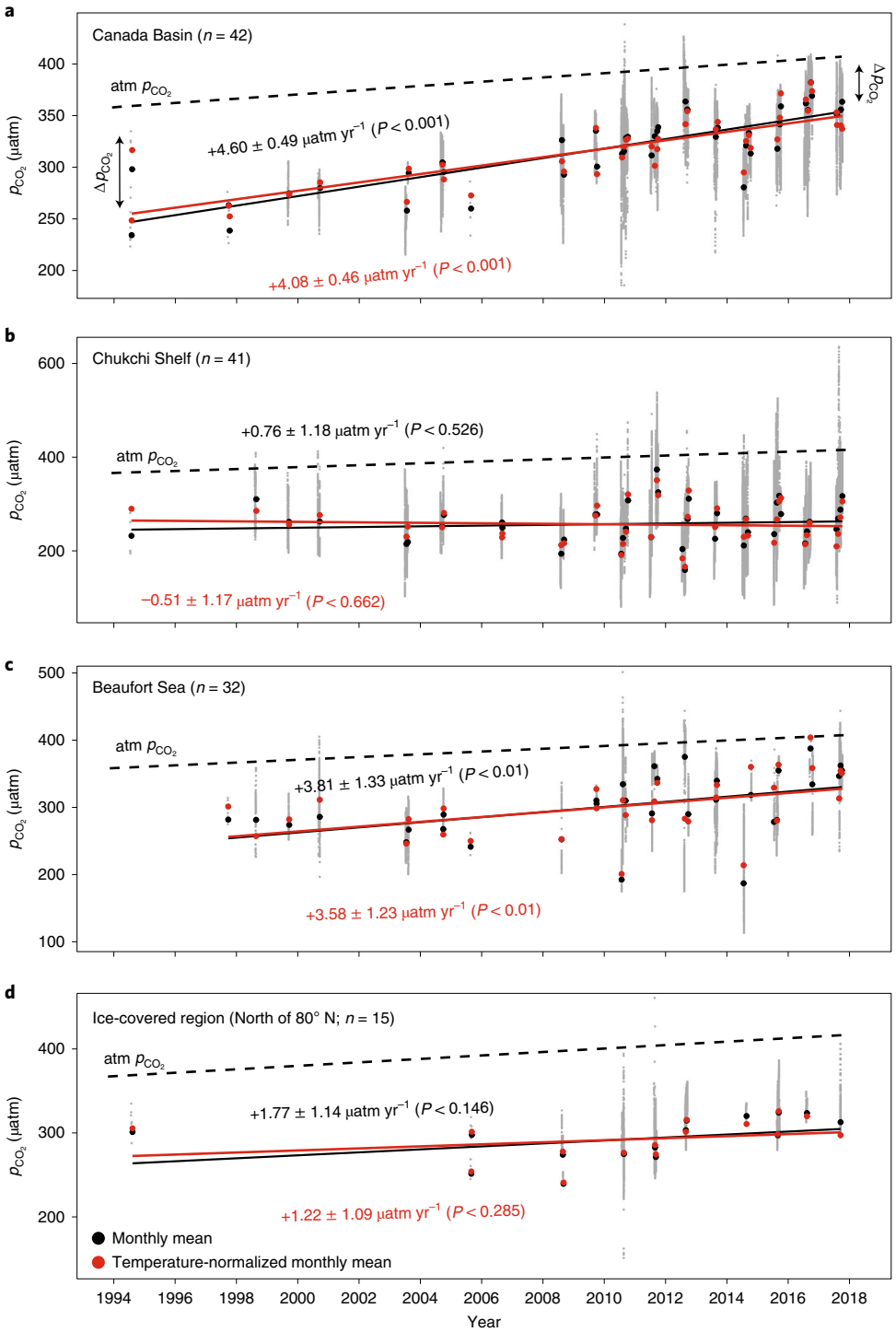

Fig. 2 | Decadal change trends of sea surface p_{CO_2} in the western Arctic Ocean. a–d, The grey dots represent the raw observations of p_{CO_2} in the Canada Basin (**a**), the Chukchi Shelf (**b**), the Beaufort Sea (**c**) and the high latitudes (north of 80° N) (**d**). The black and red dots indicate the monthly means based on the gridded-average p_{CO_2} (0.1° latitude × 0.25° longitude) at in situ SST and the long-term means of SST, respectively. The rates of change with standard errors are computed from the monthly means. *n* is the number of monthly mean values used. The solid black lines indicate the results of a linear least squares regression and red lines represent the non-thermal component of the total p_{CO_2} trends (Methods). The dashed lines represent the atmospheric CO_2 increasing at a mean rate of 1.9 µatm yr^{-1}. We tested whether the trends were significantly different from 0 using analysis of variance (ANOVA) and whether the trends were significantly different from the trend of atmospheric CO_2 using analysis of covariance. Only the trend of sea surface p_{CO_2} observed in the Canada Basin is significantly different from the trend of atmospheric p_{CO_2}. The arrows in **a** indicate the statistically significant change in Δp_{CO_2} (also see Extended Data Fig. 4).

tial increase in the Canada Basin but not the Chukchi Shelf (red lines in Fig. 2; Table 1). Thus, the dominant mechanisms controlling p_{CO_2} in these two regions are different.

Given the fact that both warming and atmospheric CO_2 uptake are driving p_{CO_2} to rise, we suggest that biological CO_2 drawdown is responsible for counteracting any discernible long-term increase

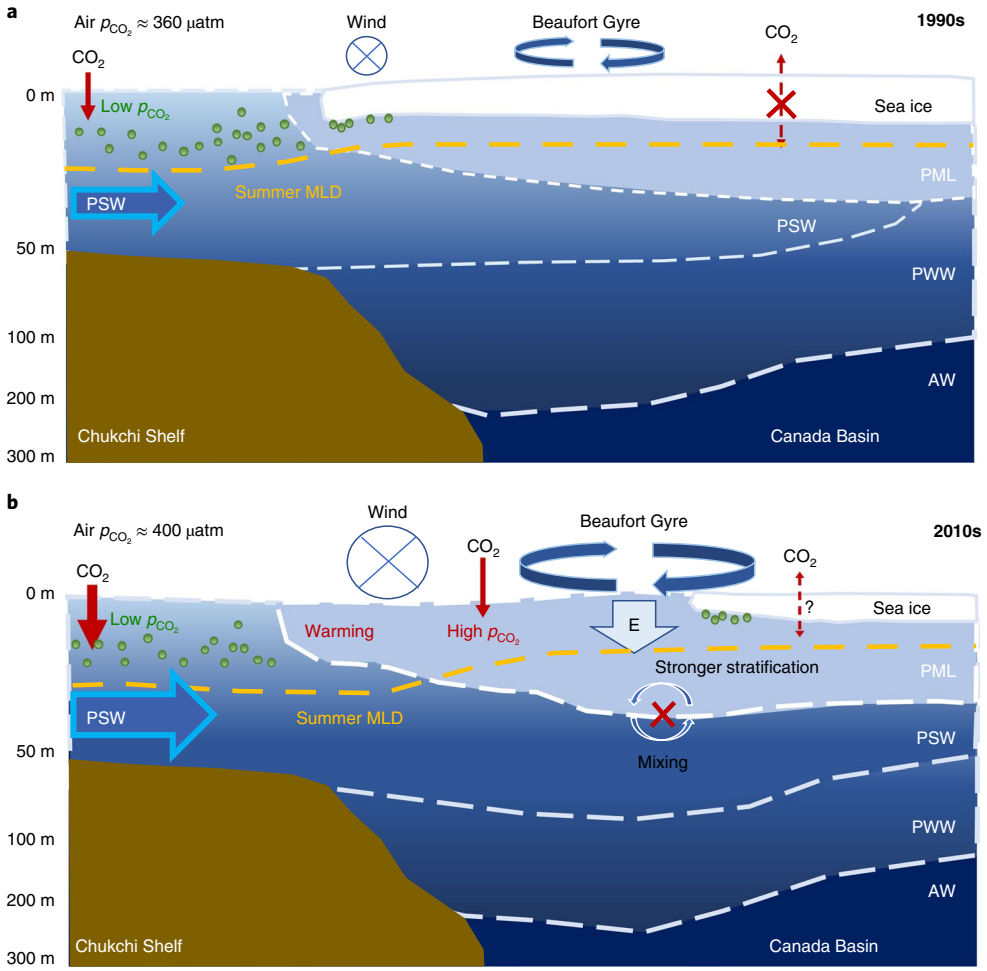

Fig. 3 | Schematic representation of recent environmental changes in the western Arctic during the ice-melt season. a,**b**, The changes in physical setting in the upper ocean along the Chukchi Shelf to the Canada Basin in the 1990s (**a**) and 2010s (**b**). Over the past few decades, amplified warming in the polar region caused rapid sea-ice retreat and changes in the circulation in the upper ocean. Increased Pacific summer water (PSW) flows through the Chukchi Shelf and subducts into the Beaufort Sea slope and the Canada Basin along the corresponding isopycnals. Stronger summer westward wind strengthens the Beaufort Gyre in the Canada Basin, which results in a stronger Ekman pumping and convergence (indicated by the arrow labelled E). The upper water column was depressed and built up a stronger stratification due to the combination of the accumulation of surface ice melt water and the stronger Ekman pumping[2]. The yellow dashed lines indicate the summer mixed layer depth (MLD), which is shallowing from spring to summer and becomes shallower in the basin than on the shelf. PML, polar mixed layer; PWW, Pacific winter water; AW, Atlantic water.

on the Chukchi Shelf. To examine this postulation further, we used a one-dimensional (1-D) box model to investigate how net community production (NCP) could affect the long-term p_{CO_2} trend (Methods). We found that a high NCP (>10 mmol C m^{-2} d^{-1}) is essential for maintaining the low p_{CO_2} values on the shelf (Supplementary Fig. 3). The patchy and widely variable primary production[24] is probably responsible for the observed high seasonal and interannual variabilities (Fig. 2b). Furthermore, after moderately increasing NCP by 30% since 2007 in our simulation (Methods) as suggested by satellite observations[8], the impacts of warming and CO_2 invasion from the atmosphere on increasing p_{CO_2} are nearly balanced, resulting in a relatively low p_{CO_2} value through the entire summer and no discernible long-term trend (Fig. 4a,b). If this summer pattern persists in the future and earlier ice melt and longer growth periods for autotrophs occur as anticipated[33], we predict that the Chukchi Shelf will be a greater CO_2 sink as atmospheric CO_2 continues to increase.

By considering the changes in the thermodynamics of the CO_2 system in the surface seawater, we can also quantify the drivers for the p_{CO_2} trend in the Canada Basin (Methods). The sea surface warming rate of 0.05 °C yr^{-1} over 1982–2015 (ref. [34]) directly results in an increase in sea surface p_{CO_2} by 0.7 µatm yr^{-1} in the Canada Basin, which corroborates the contribution of the thermal component of 0.6 µatm yr^{-1} derived from the observations (Table 1). The rest is non-thermal component and can be decomposed into two drivers. The first driver is associated with the long-term increase in surface DIC. The second driver is associated with the long-term increase in freshwater input due to sea-ice melt, which not only dilutes the surface salinity but also affects the carbonate chemistry (Methods).

Our decomposition reveals that the net increase in DIC in the surface of the Canada Basin could lead to an increase in p_{CO_2} of 6.1–6.9 µatm yr^{-1}, while freshwater input lowers the increase rate by −2.0 to −3.4 µatm yr^{-1} (last column in Table 1). As a net result, the non-thermal component increases p_{CO_2} by 2.7–4.9 µatm yr^{-1}, which contributes about 80% to 88% of the total p_{CO_2} long-term trend in the Canada Basin (Table 1).

While the non-thermal component explains most of the trend, it is still unclear which mechanism mainly drives the long-term DIC increase. The most likely one is natural and anthropogenic CO_2 uptake induced by sea-ice loss. We used a 1-D box model to simulate

Table 1 | Estimated contributions to the long-term p_{CO_2} trends in the Chukchi Shelf and the Canada Basin

	Chukchi Shelf	Canada Basin				
	Rate of change (μatm yr^{-1})	Rate of change (μatm yr^{-1})	Driver	Driver rate of change	Change in drivers (1994–2017)	Contribution to the long-term trends (μatm yr^{-1})
Thermal component	1.25 ± 0.57*	0.57 ± 0.26*	ΔSST[34]	0.05 ± 0.03* °C yr^{-1}	1.15 ± 0.69 °C	0.68
Non-thermal component	−0.51 ± 1.17	4.08 ± 0.46***	ΔsDIC	2.56 ± 1.24†* 2.28 ± 1.17‡ μmol kg^{-1} yr^{-1}	58.9 ± 28.52† 54.44 ± 26.91‡ μmol kg^{-1}	6.13–6.89
			ΔSSS	−0.10 ± 0.02*** (−0.17 ± 0.04)* ppt yr^{-1}	−2.30 ± 0.46 (−3.91 ± 0.92) ppt	−1.99 (−3.39)
Sum	0.74	4.65				4.82–5.58 (3.42–4.18)

The thermal component and non-thermal component were separated by normalizing the observed p_{CO_2} to the long-term summer mean SST. The rates (± standard error of slope) were estimated by linear regression using the monthly means. For the Chukchi Shelf, only rates of change were provided. For the Canada Basin, the drivers were further analysed. The asterisks indicate the levels of significance of the trends (***$P < 0.001$, **$P < 0.01$, *$P < 0.05$). The † and ‡ symbols indicate the change rate in sDIC normalized by using zero-concentration and non-zero-concentration freshwater endmembers, respectively. The numbers in the brackets indicate the results derived from a larger decrease in salinity (Methods). Parts per thousand (ppt) measures the salt content in seawater.

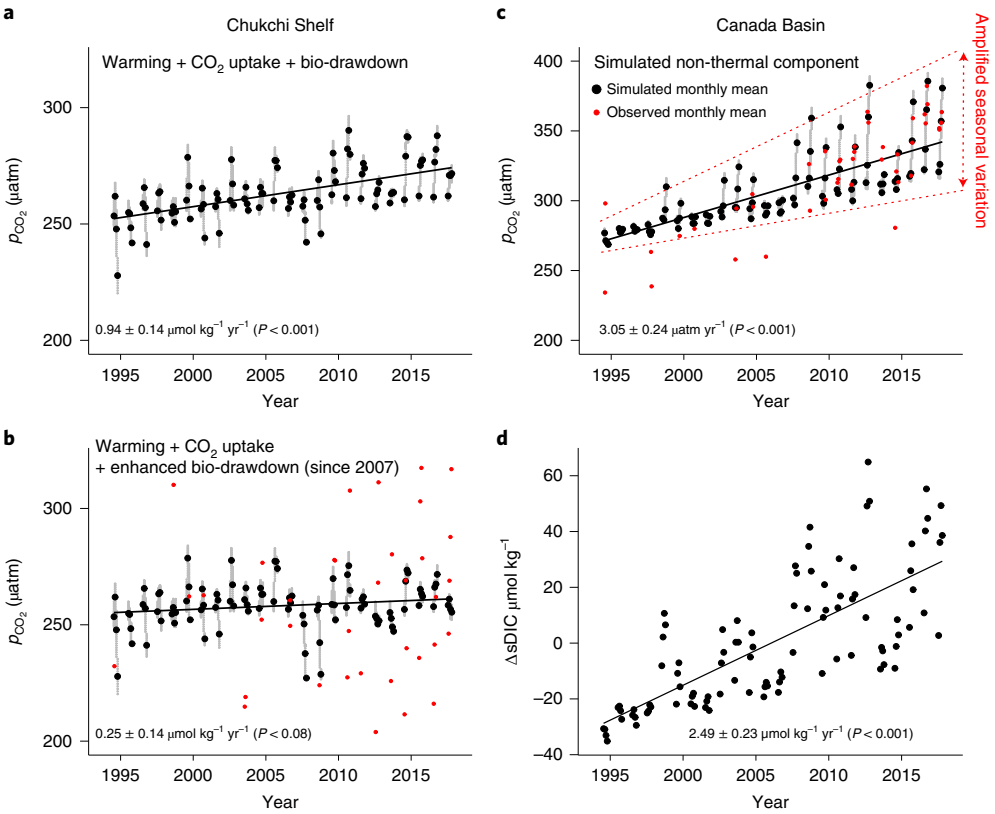

Fig. 4 | Simulation of sea surface p_{CO_2} in the Chukchi Shelf and the Canada Basin. a,**b**, Simulated summer (1 July–15 October) p_{CO_2} on the Chukchi Shelf driven by warming, CO_2 uptake and biological CO_2 drawdown (**a**), and driven by warming, CO_2 uptake, and increased biological CO_2 drawdown (**b**). We applied an increased NCP of 30% (ref. [8]) since 2007 (see Methods for the simulation conditions). **c**, The simulated p_{CO_2} in the Canada Basin is driven mainly by CO_2 uptake from atmosphere CO_2 associated with sea-ice melting processes. To examine only the non-thermal component effect, we used a long-term mean of SST and kept the weak biological CO_2 drawdown rate constant (see Methods for the simulation conditions). The grey dots represent the simulated daily p_{CO_2}. The rates of change (± standard error of slope) were computed using the monthly means (black dots). The red dots are observed monthly means. **d**, The change in sDIC anomaly (ΔsDIC) with respect to the long-term mean of sDIC. An ANOVA was performed to test whether the slopes are significantly different from 0.

seasonal p_{CO_2} evolution associated with the changing sea-ice concentration (ice%) and estimate the change in salinity-normalized DIC (sDIC) (Methods). Our simulation suggests that summer sea-ice loss in the Canada Basin has accelerated atmospheric CO_2 uptake (Fig. 4c), leading to a net increase in DIC in the surface ocean of 2.5 ± 0.2 μmol kg^{-1} yr^{-1} (Fig. 4d), which corroborates

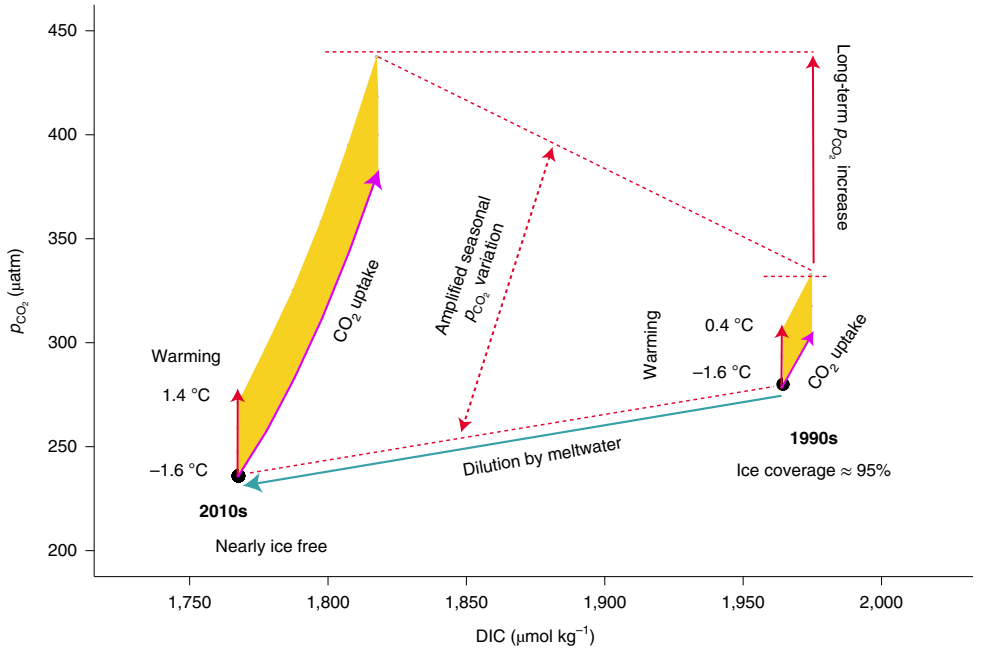

Fig. 5 | Sea-ice loss amplifying surface water p_{CO_2} in the Canada Basin. The back dots represent the initial conditions for p_{CO_2} and DIC at −1.6 °C. The arrows indicate the processes of warming (red), CO_2 uptake from the atmosphere (purple) and dilution by ice melt water (cyan). Sea-ice reduction from 95% to ice free is accompanied by a salinity decrease of 3.5 (Supplementary Table 4). The yellow shaded areas indicate the possible seasonal variations of p_{CO_2}, which are amplified by the synergistic effect of ice melt, warming and CO_2 uptake. To examine the change of p_{CO_2}, we allowed 2 °C and 3 °C warming, and 10 and 50 μmol kg^{-1} DIC perturbations due to air–sea CO_2 exchange in the 1990s and 2010s, respectively, which are consistent with the long-term warming rate of 0.5 °C per decade[34] and the estimated increase in sDIC of 2.3–2.6 μmol kg^{-1} yr^{-1} (Table 1 and Fig. 4d).

the observational rates of 2.3–2.6 μmol kg^{-1} yr^{-1} (Extended Data Fig. 5b,e). This agreement supports our proposed mechanism that increased air–sea CO_2 uptake due to sea-ice loss is primarily responsible for the net DIC increase, and hence for most of the observed long-term sea surface p_{CO_2} rise. Although more accurate estimates may be obtained with improved models and increased observations, they would not substantially change our mechanistic understanding.

The simulated p_{CO_2} implies that the decline in ice% in the Canada Basin not only promotes CO_2 uptake but also results in an amplification of the seasonal variability of p_{CO_2} (Fig. 4c), particularly when combined with seasonal SST forcing. This synergistic effect resulting from warming, ice melt dilution and atmospheric CO_2 uptake on seawater p_{CO_2} is illustrated in Fig. 5. As summer ice% rapidly decreased over the 1990s–2010s, the seasonal SST amplitude increased due to the positive albedo-warming feedback[35,36]. Expanded open-water area promoted CO_2 uptake, and diluted seawater, with a lower initial p_{CO_2}, allowed a larger DIC increase (Fig. 5). We suggest that this rapid DIC increase in diluted water would lead to a rapid increase of the dissolved CO_2 fraction in DIC, an increase in the DIC/Alk ratio and a decrease in the acid–base buffer capacity (Extended Data Fig. 6). In turn, water with a lower buffer capacity has a larger and disproportionate p_{CO_2} increase when responding to any further DIC perturbation. Together, these processes lead to a larger summer p_{CO_2} variation[37] and a faster long-term summertime p_{CO_2} trend (Fig. 5).

Arctic Ocean sea-ice loss, a critical consequence of climate change associated with a fresher and isolated surface mixed layer, serves as an amplifier of the seasonal variation and decadal increase of p_{CO_2} in the Canada Basin. In contrast to the thermal and biophysical effects that dominate the p_{CO_2} seasonal cycles in the low and mid-latitudes, the subarctic seas and most of the Southern Ocean[16,17,30,32], the sea-ice melt cycle in the Arctic Ocean operates as a unique mechanism and magnifies changes in p_{CO_2} over seasonal to decadal scales. The accelerated sea-ice loss anticipated in the near future[33] will increase seasonal variations in sea surface p_{CO_2}, decrease the CO_2 sink in the Canada Basin and increase it on the Chukchi Shelf, and increase the long-term ocean acidification rates in the Arctic Ocean, which may profoundly affect the carbon cycle, biogeochemical dynamics and ecosystem functions.

Online content

Any methods, additional references, Nature Research reporting summaries, source data, extended data, supplementary information, acknowledgements, peer review information; details of author contributions and competing interests; and statements of data and code availability are available at https://doi.org/10.1038/s41558-020-0784-2.

Received: 23 March 2019; Accepted: 22 April 2020;
Published online: 15 June 2020

References

1. Onarheim, I. H., Eldevik, T., Smedsrud, L. H. & Stroeve, J. C. Seasonal and regional manifestation of Arctic sea ice loss. *J. Climate* **31**, 4917–4932 (2018).
2. Stroeve, J. & Notz, D. Changing state of Arctic sea ice across all seasons. *Environ. Res. Lett.* **13**, 103001 (2018).
3. Giles, K. A., Laxon, S. W., Ridout, A. L., Wingham, D. J. & Bacon, S. Western Arctic Ocean freshwater storage increased by wind-driven spin-up of the Beaufort Gyre. *Nat. Geosci.* **5**, 194–197 (2012).
4. Yamamoto-Kawai, M. et al. Surface freshening of the Canada Basin, 2003-2007: river runoff versus sea ice meltwater. *J. Geophys. Res. Oceans* **114**, C00A05 (2009).
5. Timmermans, M.-L. et al. Mechanisms of Pacific summer water variability in the Arctic's central Canada Basin. *J. Geophys. Res. Oceans* **119**, 7523–7548 (2014).
6. Corlett, W. B. & Pickart, R. S. The Chukchi slope current. *Prog. Oceanogr.* **153**, 50–65 (2017).
7. Stabeno, P., Kachel, N., Ladd, C. & Woodgate, R. Flow patterns in the Eastern Chukchi Sea: 2010–2015. *J. Geophys. Res. Oceans* **123**, 1177–1195 (2018).
8. Arrigo, K. R. & van Dijken, G. L. Continued increases in Arctic Ocean primary production. *Prog. Oceanogr.* **136**, 60–70 (2015).

9. Yamamoto-Kawai, M., McLaughlin, F. A., Carmack, E. C., Nishino, S. & Shimada, K. Aragonite undersaturation in the Arctic Ocean: effects of ocean acidification and sea ice melt. *Science* **326**, 1098–1100 (2009).
10. Qi, D. et al. Increase in acidifying water in the western Arctic Ocean. *Nat. Clim. Change* **7**, 195–201 (2017).
11. Robbins, L. L. et al. Baseline monitoring of the western Arctic Ocean estimates 20% of Canadian Basin surface waters are undersaturated with respect to aragonite. *PLoS ONE* **8**, e73796 (2013).
12. Anderson, L. G. et al. Export of calcium carbonate corrosive waters from the East Siberian Sea. *Biogeosciences* **14**, 1811–1823 (2017).
13. Coupel, P. et al. The impact of freshening on phytoplankton production in the Pacific Arctic Ocean. *Prog. Oceanogr.* **131**, 113–125 (2015).
14. Nishino, S. et al. Enhancement/reduction of biological pump depends on ocean circulation in the sea ice reduction regions of the Arctic Ocean. *J. Oceanogr.* **67**, 305–314 (2011).
15. Cai, W.-J. et al. Decrease in the CO_2 uptake capacity in an ice-free Arctic Ocean basin. *Science* **329**, 556–559 (2010).
16. Takahashi, T. et al. Climatological mean and decadal change in surface ocean p_{CO_2}, and net sea–air CO_2 flux over the global oceans. *Deep Sea Res. 2* **56**, 554–577 (2009).
17. Takahashi, T. et al. Climatological distributions of pH, p_{CO_2}, total CO_2, alkalinity, and $CaCO_3$ saturation in the global surface ocean, and temporal changes at selected locations. *Mar. Chem.* **164**, 95–125 (2014).
18. Bates, N. R. et al. A time-series view of changing surface ocean chemistry due to ocean uptake of anthropogenic CO_2 and ocean acidification. *Oceanography* **27**, 126–141 (2014).
19. Bates, N. R., Moran, S. B., Hansell, D. A. & Mathis, J. T. An increasing CO_2 sink in the Arctic Ocean due to sea-ice loss. *Geophys. Res. Lett.* **33**, 1–7 (2006).
20. Else, B. G. T. et al. Further observations of a decreasing atmospheric CO_2 uptake capacity in the Canada Basin (Arctic Ocean) due to sea ice loss. *Geophys. Res. Lett.* **40**, 1132–1137 (2013).
21. Woodgate, R. A., Weingartner, T. J. & Lindsay, R. Observed increases in Bering Strait oceanic fluxes from the Pacific to the Arctic from 2001 to 2011 and their impacts on the Arctic Ocean water column. *Geophys. Res. Lett.* **39**, L24603 (2012).
22. Woodgate, R. A. Increases in the Pacific inflow to the Arctic from 1990 to 2015, and insights into seasonal trends and driving mechanisms from year-round Bering Strait mooring data. *Prog. Oceanogr.* **160**, 124–154 (2018).
23. Hill, V., Ardyna, M., Lee, S. H. & Varela, D. E. Decadal trends in phytoplankton production in the Pacific Arctic Region from 1950 to 2012. *Deep Sea Res. 2* **152**, 82–94 (2018).
24. Grebmeier, J. M. et al. Ecosystem characteristics and processes facilitating persistent macrobenthic biomass hotspots and associated benthivory in the Pacific Arctic. *Prog. Oceanogr.* **136**, 92–114 (2015).
25. Spall, M. A. et al. Transport of Pacific water into the Canada Basin and the formation of the Chukchi slope current. *J. Geophys. Res. Oceans* **123**, 7453–7471 (2018).
26. Brugler, E. T. et al. Seasonal to interannual variability of the Pacific water boundary current in the Beaufort Sea. *Prog. Oceanogr.* **127**, 1–20 (2014).
27. Peralta-Ferriz, C. & Woodgate, R. A. Seasonal and interannual variability of pan-Arctic surface mixed layer properties from 1979 to 2012 from hydrographic data, and the dominance of stratification for multiyear mixed layer depth shoaling. *Prog. Oceanogr.* **134**, 19–53 (2015).
28. Mathis, J. T. et al. Storm-induced upwelling of high p_{CO_2}waters onto the continental shelf of the western Arctic Ocean and implications for carbonate mineral saturation states. *Geophys. Res. Lett.* **39**, L07606 (2012).
29. Takahashi, T., Olafsson, J., Goddard, J. G., Chipman, D. W. & Sutherland, S. C. Seasonal variation of CO_2 and nutrients in the high-latitude surface oceans: a comparative study. *Glob. Biogeochem. Cycles* **7**, 843–878 (1993).
30. Takahashi, T. et al. Global sea–air CO_2 flux based on climatological surface ocean p_{CO_2}, and seasonal biological and temperature effects. *Deep Sea Res. 2* **49**, 1601–1622 (2002).
31. Lovenduski, N. S., Gruber, N., Doney, S. C. & Lima, I. D. Enhanced CO_2 outgassing in the Southern Ocean from a positive phase of the Southern Annular Mode. *Glob. Biogeochem. Cycles* **21**, GB2026 (2007).
32. Landschützer, P., Gruber, N., Bakker, D. C., Stemmler, I. & Six, K. D. Strengthening seasonal marine CO_2 variations due to increasing atmospheric CO_2. *Nat. Clim. Change* **8**, 146–150 (2018).
33. Wang, M., Yang, Q., Overland, J. E. & Stabeno, P. Sea-ice cover timing in the Pacific Arctic: the present and projections to mid-century by selected CMIP5 models. *Deep Sea Res. 2* **152**, 22–34 (2018).
34. Timmermans, M.-L., Ladd, C. & Wood, K. *Sea Surface Temperature* (Arctic Report Card, NOAA, 2015).
35. Steele, M. & Dickinson, S. The phenology of Arctic Ocean surface warming. *J. Geophys. Res. Oceans* **121**, 6847–6861 (2016).
36. Perovich, D. K. & Polashenski, C. Albedo evolution of seasonal Arctic sea ice. *Geophys. Res. Lett.* **39**, L08501 (2012).
37. DeGrandpre, M. et al. Changes in the Arctic Ocean carbon cycle with diminishing ice cover, *Geophys. Res. Lett.* Preprint at https://www.essoar.org/doi/10.1002/essoar.10502603.1 (2020).

Methods

The synthesis of the p_{CO_2} dataset. To examine decadal changes in surface p_{CO_2} and estimate the summer carbon uptake in the western Arctic Ocean, we synthesized a dataset of p_{CO_2} measurements via multiple international databases (Supplementary Table 1), including the Surface Ocean CO_2 Atlas[38] (SOCAT v.5, http://www.socat.info), Japan Agency for Marine-Earth Science and Technology (JAMSTEC, https://www.jamstec.go.jp/e/), Carbon Dioxide Information Analysis Center (CDIAC, https://cdiac.ess-dive.lbl.gov), USGS database (https://pubs.er.usgs.gov), LDEO Database Version 2017 (ref. [39]) (https://www.nodc.noaa.gov/ocads/data/0160492.xml), NSF Arctic Data Center (https://arcticdata.io) and Chinese National Arctic and Antarctic Data Center (http://www.chinare.org.cn). This extensive dataset contains more than 358,000 sea surface p_{CO_2} data points and associated SST and sea surface salinity (SSS) data. All the data are archived in publicly accessible databases (Supplementary Table 1), and the entire dataset is provided in the Supplementary Information.

Underway sea surface p_{CO_2} data. During 2008, 2010, 2012, 2014, 2016 and 2017 cruises of the Chinese Arctic Research Expedition (CHINARE), the sea surface underway p_{CO_2} was measured with a non-dispersive infrared analyser in the equilibrated headspace gas by an underway CO_2 system (General Oceanics). The system was monitored and calibrated with four certified gas standards every 3 h, which could provide an overall precision of ±2 µatm in p_{CO_2} measurements. The underway CO_2 system and the data reduction procedure are described in ref. [40]. Combined with the historical and recent measurements from multiple international programmes, we retained only the data from the sea-ice melting season (1 July –15 October) for the data synthesis. To maintain data consistency, we chose to report and analyse all the data as p_{CO_2}; thus, the reported CO_2 fugacity (f_{CO_2}) from some programmes (Supplementary Table 1) was converted to p_{CO_2} at SST using equation (1) (ref. [39]):

$$p_{CO_2} = f_{CO_2} \times \left(1.00436 - 4.669 \times 10^{-5} \times \mathrm{SST}\right) \quad (1)$$

Note that the difference between p_{CO_2} and f_{CO_2} is less than the measurement precision of ±2 µatm; thus, the error induced by the conversion is negligible.

Discrete sea surface p_{CO_2} data. The p_{CO_2} datasets of Arctic Ocean Section 1994 (AOS 1994), Joint Ocean Ice Study 1997 (JOIS 1997), Surface Heat budget of the Arctic Ocean 1998 (SHEBA 1998) and Beringia 2005: Ecology and Evolution (ODEN 2005) were calculated from the discrete DIC and Alk samples taken in the surface mixed layer (<20 m). The DIC and Alk values were calibrated with deep water before the calculation[10]. The p_{CO_2} was calculated by the CO2SYS program[41] with dissociation constants from[42]. The uncertainty of p_{CO_2} values computed from Alk and DIC is about ±13 µatm with a mean systematic difference from the measured p_{CO_2} of –0.7 µatm (ref. [43]).

Sea surface p_{CO_2} trends assessment. Although the assembled dataset has extensive measurements, the temporal and spatial coverage of p_{CO_2} varies greatly with months and years. Before identifying the long-term trends of p_{CO_2}, we examined the temporal distribution of p_{CO_2} measurements for each subregion (Extended Data Fig. 2). We noticed that the number of p_{CO_2} observations for each month could vary greatly among years depending on the number and timing of cruises, and the sea-ice conditions in a particular year. For example, the number of p_{CO_2} values substantially increased after 2007 (Extended Data Fig. 2). Thus, simple linear regressions with the raw data could amplify the sampling bias due to an uneven spread of seasonal p_{CO_2} measurements. Despite the statistically significant P value, the raw data is not a good candidate for the assessment of long-term trends (Supplementary Table 2). One way to reduce this bias is to average the p_{CO_2} measurements into specific temporal intervals (such as daily, monthly or summer means) and then examine the long-term trends with these temporal-averaged values. We found that the rates derived from the summer means (which include all data measured from 1 July to 15 October) are much lower than those from the daily and monthly means, which indicates that simply averaging p_{CO_2} measurements into a summer mean may not be a good approach due to losing too much seasonal information. However, the rates derived from the daily and monthly means tend to be close to each other (Supplementary Table 2).

Another issue with the p_{CO_2} observations is spatially unevenly distributed sampling, which may induce bias from the overweighted impact of highly dense data points concentrated within a small area. To deal with this issue, we averaged all the data points into grids. We examined different grid sizes (0.1° latitude × 0.25° longitude and 0.25° latitude × 0.5° longitude) for averaging into a daily mean, a monthly mean and a summer mean (Supplementary Table 2). The two grid sizes we applied led to consistent p_{CO_2} trends in all subregions. Here we choose to report the long-term p_{CO_2} trends with gridded-averaged (0.1° latitude × 0.25° longitude) monthly means. By doing this, we not only reduce sampling bias in spatial coverage but also retain more temporal information, considering the scarcity of p_{CO_2} measurements in the Arctic Ocean. We test whether the trends are significantly different from 0 using ANOVA.

We further examined the seasonality of the p_{CO_2} by plotting p_{CO_2} on Julian days for each subregion (Extended Data Fig. 3a–h). We noticed that, unlike the relatively static year-by-year seasonality in low- and temperate-latitude oceans[16,32], the seasonality of p_{CO_2} in the Arctic Ocean is susceptible to perturbations of the sea-ice melting cycle, which may vary greatly among years. This unique seasonal driver could result in the shift in p_{CO_2} seasonality as the ice-free area has extended into the Canada Basin since 2007. We demonstrated the possible change in the p_{CO_2} seasonality in different subregions by examining the seasonal evolution of p_{CO_2} in two periods (before and after 2007; Extended Data Fig. 3). Clearly, except for the ice-covered area (north of 80° N), the seasonality of p_{CO_2} in most of our study area has changed in both magnitude and amplitude. Bearing this in mind, we carefully compared the deseasonalized trends with the non-deseasonalized results (Extended Data Fig. 3i–l), assuming that the climatological mean seasonality remained unchanged over this period, using the method described in ref. [16]. Although we found that the long-term trend of p_{CO_2} increased after seasonal adjustment in the Beaufort Sea, the deseasonalized trends in other subregions were within the uncertainties of the presented trends. We were also concerned that the deseasonalization of p_{CO_2} in the Arctic Ocean may induce extra bias, as the current synthesized p_{CO_2} data with limited seasonal coverage cannot reflect a completed seasonal cycle. We therefore reported p_{CO_2} trends without deseasonalization here.

To examine whether the observed p_{CO_2} trends are significantly different from the atmospheric CO_2 trend, we conducted an analysis of covariance for each subregion. Only the trend of sea surface p_{CO_2} observed in the Canada Basin was found to be significantly different from the trend of atmospheric CO_2, which supports our finding that the summer sea surface p_{CO_2} trend in the Canada Basin is significantly higher than that of the atmospheric CO_2.

Uncertainty analysis of the long-term trends. As we mentioned above, the current synthesized p_{CO_2} dataset is inhomogeneously distributed over time and space, which contributes to the uncertainty of the reported trends in sea surface p_{CO_2}. The uncertainty is also closely associated with the account of measurements used for deriving the long-term trend in each subregion.

To quantify the uncertainty of the p_{CO_2} trends, we conducted a sensitivity test by randomly removing 15% of the cruises or 15% of the measurements from the raw dataset and gridded the data with a grid size of 0.1° latitude × 0.25° longitude for averaging the monthly means for every year, and we then re-examined the slope of regression. By repeating this process 100 times, we found that both approaches gave similar results (Supplementary Fig. 1), but the derived p_{CO_2} trends were more sensitive to the removal of cruises than the removal of data points. We also noticed that the regionally varying sensitivities depend on the total number of cruises or data points. For example, the ice-covered region with the lowest numbers of cruises and measurements was more sensitive in responding to any change in this unevenly sampled dataset than the other three subregions (Supplementary Fig. 1). We ran a second test by randomly removing 30% of the cruises or measurements (Supplementary Fig. 2). This test resulted in similar trends as the first test but with larger standard deviations. This indicated that adding or removing measurements only slightly increased the uncertainty but did not significantly change the trends. Here we report the uncertainty of the long-term p_{CO_2} trends with the standard deviation of the mean of 100 slopes (Supplementary Figs. 1 and 2). For the Canada Basin and the Beaufort Sea, the relative uncertainties (s.d./mean) of p_{CO_2} are less than 8% and 15%, respectively, whereas the uncertainties could reach as high as 65%–75% in the Chukchi Shelf and the ice-covered region.

Separation of the thermal and non-thermal components. We separate the observation-based p_{CO_2} into the thermal component, which is driven by the seasonal and long-term variation in SST, and the non-thermal component, which is driven by the seasonal and long-term variation in all other factors, including DIC, Alk and salinity. To calculate the thermal component, we first calculated the summer mean of p_{CO_2}, $<p_{CO_2}>_{summer}$, with the gridded data for each year, and then perturbed $<p_{CO_2}>_{summer}$ with the SST differences between the observed SST and the 23-year long-term mean SST, <SST>, and the temperature sensitivity of CO_2 (γ_T) of 4.23% °C^{-1} (ref. [29]), as follows:

$$p_{CO_2\,\mathrm{thermal}} = <p_{CO_2}>_{\mathrm{summer}} \times \exp(\gamma_T \times (\mathrm{SST} - <\mathrm{SST}>)) \quad (2)$$

The non-thermal component was calculated by normalizing the observed p_{CO_2} to <SST> to remove the temperature effect [30], as follows:

$$p_{CO_2\,\mathrm{non-thermal}} = p_{CO_2} \times \exp(\gamma_T \times (<\mathrm{SST}> - \mathrm{SST})) \quad (3)$$

The separation of the two components of the observed p_{CO_2} is shown in Table 1.

Drivers of the long-term p_{CO_2} trends. To determine the potential drivers of the long-term trends in observed p_{CO_2} in the Arctic Ocean, we decomposed the variation of p_{CO_2} into multiple components: SST, SSS, DIC and Alk. Therefore, the change in p_{CO_2}, dp_{CO_2}, could be expressed as:

$$dp_{CO_2} = \frac{\partial p_{CO_2}}{\partial \mathrm{SST}} \times d\mathrm{SST} + \frac{\partial p_{CO_2}}{\partial \mathrm{DIC}} \times d\mathrm{DIC} + \frac{\partial p_{CO_2}}{\partial \mathrm{Alk}} \times d\mathrm{Alk} + \frac{\partial p_{CO_2}}{\partial \mathrm{SSS}} \times d\mathrm{SSS} \quad (4)$$

where d indicates the deviation of the property from the respective norm. As freshwater (fw) fluxes can also induce changes in DIC and Alk, it is often useful to separate the freshwater influence from other biogeochemical processes

by calculating salinity-normalized DIC (sDIC) and Alk (sAlk). We used sDIC ($DIC \times S_0/SSS$) and sAlk ($Alk \times S_0/SSS$) to substitute the terms in equation (4) and combined all terms affected by freshwater fluxes into one term[29,31,32]. SSS and S_0 represent the observed and reference salinity. Here, S_0 is taken as the summer mean salinity. This gives

$$\begin{aligned} dp_{CO_2} = {} & \frac{\partial p_{CO_2}}{\partial SST} \times dSST + \frac{\partial p_{CO_2}}{\partial DIC} \times SSS/S_0 \times dsDIC + \frac{\partial p_{CO_2}}{\partial Alk} \times SSS/S_0 \\ & \times dsAlk + \frac{\partial p_{CO_2}}{\partial fw} \times dfw \end{aligned} \quad (5)$$

$$\frac{\partial p_{CO_2}}{\partial fw} \times dfw = \left(\frac{sDIC}{S_0} \frac{\partial p_{CO_2}}{\partial DIC} + \frac{sAlk}{S_0} \frac{\partial p_{CO_2}}{\partial Alk} + \frac{SSS}{S_0} \frac{\partial p_{CO_2}}{\partial SSS} \right) \times dSSS \quad (6)$$

We estimated the regional mean values of the partial derivatives of p_{CO_2} with the following approximating equations, expressed as the p_{CO_2} sensitivities, γ, with regard to the respective drivers[44] (γ_{DIC}, γ_{Alk}, and γ_{SSS} are the p_{CO_2} sensitivities for DIC, Alk and salinity, respectively).

$$\frac{\partial p_{CO_2}}{\partial DIC} = \frac{p_{CO_2}}{DIC} \times \gamma_{DIC} \quad (7)$$

$$\frac{\partial p_{CO_2}}{\partial Alk} = \frac{p_{CO_2}}{Alk} \times \gamma_{Alk} \quad (8)$$

$$\frac{\partial p_{CO_2}}{\partial SSS} = \frac{p_{CO_2}}{SSS} \times \gamma_{SSS} \quad (9)$$

By substituting equations (7)–(9) into equation (6), we get

$$\frac{\partial p_{CO_2}}{\partial fw} \times dfw = \frac{p_{CO_2}}{S_0} (\gamma_{DIC} + \gamma_{Alk} + \gamma_{SSS}) dSSS \quad (10)$$

As we are considering deviations from the summer mean, SSS/S_0 in equations (5) and (6) approximates to 1 and can be dropped. With this simplification, we replaced d with the long-term change in summer p_{CO_2}, $\Delta^{LT} p_{CO_2}$:

$$\begin{aligned} \Delta^{LT} p_{CO_2} = {} & \Delta^{LT} p_{CO_2\,thermal} + \Delta^{LT} p_{CO_2\,non-thermal} \\ = {} & (\gamma_T \times \Delta^{LT} SST \times p_{CO_2}) + (\gamma_{DIC} \times \frac{p_{CO_2}}{DIC} \times \Delta^{LT} sDIC) \\ & + (\gamma_{Alk} \times \frac{p_{CO_2}}{Alk} \times \Delta^{LT} sAlk) + ((\gamma_{DIC} + \gamma_{Alk} + \gamma_{SSS}) \times \frac{p_{CO_2}}{S_0} \times \Delta^{LT} SSS) \end{aligned} \quad (11)$$

Equation (11) represents the long-term change in p_{CO_2} and is driven by two components: the thermal component (the first term of the right side) and the non-thermal component (the remaining three terms). The above approach has been used extensively in analysing the key processes controlling surface p_{CO_2} variations in the global ocean and various ocean regions[29,31,32,44].

For further analysis, we focused on quantifying the contribution of each component to the long-term p_{CO_2} trend in the Canada Basin. We started by examining the long-term changes in sDIC, sAlk and SSS in our study regions with the discrete DIC, Alk samples and underway measurements of SSS during multiple cruises over 1994–2016. The discrete DIC and Alk data were obtained from the Global Data Analysis Project version 2 database 2019 (GLODAP v.2.2019)[45].

Considering that DIC and Alk in the sea ice also affect surface DIC and Alk when the ice melts, the salinity normalization widely used in the open ocean (described above) may not reflect the reality in the meltwater-influenced Arctic surface water. We therefore conducted a non-zero endmembers salinity normalization[46] for DIC and Alk as well to justify the potential drivers and their contributions to long-term changes in p_{CO_2}. Simply, DIC and Alk were normalized to a reference salinity (S_0) using a non-zero freshwater endmember as follows[46]:

$$sDIC = \frac{DIC - DIC_{salinity=0}}{SSS} \times S_0 + DIC_{salinity=0} \quad (12)$$

$$sAlk = \frac{Alk - Alk_{salinity=0}}{SSS} \times S_0 + Alk_{salinity=0} \quad (13)$$

The ice meltwater salinity, Alk and DIC values were set as 5 ppt, 450 μmol kg^{-1} and 400 μmol kg^{-1}, respectively[47], which are equivalent to $DIC_{salinity=0} = 60$ μmol kg^{-1} and $Alk_{salinity=0} = 104$ μmol kg^{-1}.

Both salinity normalization approaches suggest that no trend was found in sAlk in the Canada Basin (Extended Data Fig. 5a,d). We therefore dropped the sAlk term subsequently (which is the practice in the literature[32]). The non-thermal part of equation (11) thus reduces to drivers of sDIC and dfw.

$$\begin{aligned} \Delta^{LT} p_{CO_2} = {} & (\gamma_T \times \Delta^{LT} SST \times p_{CO_2}) + (\gamma_{DIC} \times \frac{p_{CO_2}}{DIC} \times \Delta^{LT} sDIC) \\ & + ((\gamma_{DIC} + \gamma_{Alk} + \gamma_{SSS}) \times \frac{p_{CO_2}}{S_0} \times \Delta^{LT} SSS) \end{aligned} \quad (14)$$

We next determined the temporal trends for each driver by deriving the temporal derivative of the long-term difference of p_{CO_2}. As we are examining the long-term trend of p_{CO_2}, the terms $\frac{p_{CO_2}}{DIC}$ and $\frac{p_{CO_2}}{S_0}$ do not change with time (though they vary within a season) and are considered as constants; thus, we get

$$\begin{aligned} \frac{d\Delta^{LT} p_{CO_2}}{dt} = {} & (\gamma_T \times p_{CO_2} \times \frac{d\Delta^{LT} SST}{dt}) \\ & + (\gamma_{DIC} \times \frac{p_{CO_2}}{DIC} \times \frac{d\Delta^{LT} sDIC}{dt}) \\ & + (\gamma_{DIC} + \gamma_{Alk} + \gamma_{SSS}) \times \frac{p_{CO_2}}{S_0} \times \frac{d\Delta^{LT} SSS}{dt} \end{aligned} \quad (15)$$

where γ_{DIC} is the long-term mean, calculated from discrete DIC and Alk using the CO2SYS program[41], and ($\gamma_{DIC} + \gamma_{Alk} + \gamma_{SSS}$) is the total p_{CO_2} sensitivity for salinity variation, which was adopted as a constant 1.7 here following the estimation for the high latitudes[29,44].

According to equation (15), the long-term trend of p_{CO_2} is attributable to three drivers. The first one is the long-term change in SST, which is primarily the result of increased absorption of solar radiation associated with sea-ice loss[36]. The second one is the change in sDIC, as a result of ocean circulation or mixing, biological activity, and natural and anthropogenic CO_2 invasion. The third driver is the long-term changes in SSS, mainly due to ice-melt water dilution and river discharge input.

Here we quantified the contribution of each component to the long-term p_{CO_2} trend. The warming trend in the summer mixed layer in the Arctic Ocean is about 0.5 ± 0.3 °C per decade from 1982 to 2015 (ref. [34]). Thus, for the thermal component, we used the warming trend of SST ($\frac{d\Delta^{LT} SST}{dt} = 0.05 \pm 0.03$ °C yr^{-1}) to estimate the thermal effect on the long-term p_{CO_2} trend (Table 1). For the non-thermal component, we estimated the long-term trends in sDIC and SSS. On the basis of the discrete DIC data obtained from GLODAP v.2.2019 (ref. [45]), we found that the sDIC in the Canada Basin increased at a rate of 2.3 ± 1.2 to 2.6 ± 1.2 μmol kg^{-1} yr^{-1} (Extended Data Fig. 5b,e). Thus, we adopted a $\frac{d\Delta^{LT} sDIC}{dt}$ of 2.3–2.6 μmol kg^{-1} yr^{-1} for the assessment. While the underway observation of SSS indicates a decrease of −1.0 ppt per decade (1994–2017; Extended Data Fig. 5g), another synthesis study (1979–2012)[27] reported an even larger salinity decrease (−1.7 ppt per decade) during the summer months. Therefore, a range of $\frac{d\Delta^{LT} SSS}{dt}$ of −0.10 to −0.17 ppt yr^{-1} was taken into consideration.

The results of equation (15) and its components are listed in Table 1.

Box model simulation of summer sea surface p_{CO_2}. To investigate the different behaviours of sea surface p_{CO_2} on the shelf and in the basin and their responses to the Arctic environmental changes, we performed a 1-D modelling exercise of seasonal change of p_{CO_2} (1 July to 15 October) from 1994 to 2017. Due to the model limitation that there is no physical circulation and no mixing components, we do not expect that such a simple model can precisely reconstruct the summer p_{CO_2} variation in the past, but we believe that this simple model effectively and sufficiently illustrates the most important processes controlling the surface water p_{CO_2}, such as warming, reduced ice concentration, enhanced biological activity and increased freshwater input. Below we first introduce the choice of parameters and then describe the simulation process.

SSS versus ice concentration. The Pacific summer water flowing through the Bering Strait was modified by mixing with the Pacific winter water, river runoff and ice melt water, which dominates the water masses on the Chukchi Shelf. For most of the period of July to October, the Chukchi has already become ice free (ice% < 15%). To simplify the analysis, we assumed that water mass circulation and mixing on the Chukchi Shelf have not changed markedly in the recent past. We thus use a constant salinity of 29.8 ppt on the Chukchi Shelf for the simulation, which is the long-term summer mean and is determined from the underway salinity measurements. In contrast, the summer ice melt water mixed with the upper polar water determines the water characters in the central basins. There is therefore a possible relationship between ice concentration and water salinity[27], which becomes more apparent in recent years as multiyear ice has been replaced by one-year ice in most of the Canada Basin[2]. We established an empirical relationship between ice concentration and salinity in the Canada Basin on the basis of the underway measurement of salinity accompanied by satellite ice concentration data. We found that there is a significant relationship between surface salinity and ice concentration averaged back to 5 d before the sampling day during the CHINARE 2016 cruise (Supplementary Fig. 4). A similar correlation was observed in a more comprehensive analysis in the Canada Basin (see Fig. 8c in ref. [27]). Thus, with ice% satellite data from 1994 to 2017, we estimated the corresponding salinity using this empirical equation for the Canada Basin surface water (Supplementary Fig. 4). It is encouraging that our salinity calculated from ice% has a decrease rate of −0.7 ppt per decade, which agrees well with the rate based on the underway observation of −1.0 ppt per decade (Extended Data Fig. 5g).

SSS versus Alk. The relationship between surface salinity and Alk is derived from the mixing curve of discrete samples obtained from GLODAP v.2.2019[45], which were sampled during multiple cruises from 1994 to 2016. We examined the relationships separately for the Chukchi Shelf and the Canada Basin due to the spatial heterogeneity of the surface water (Supplementary Fig. 5). We found two significant relationships between SSS and Alk for the respective subregions, but we did not notice any apparent shift of relationships from the early period

(before 2007) to the later period (since 2007) as the ice extent retreated northward (Supplementary Fig. 5).

Initial p_{CO_2}, DIC and Alk. On the basis of the observed p_{CO_2} in the 1990s in the Chukchi Shelf and Canada Basin (Fig. 2a,d), we set the initial p_{CO_2} at 260 µatm and 280 µatm, respectively, representing the p_{CO_2} conditions in early July or before ice melt. As we noticed that the p_{CO_2} in the ice-covered high latitudes increases at a rate of 1.8 µatm yr^{-1}, indicating a background increase in p_{CO_2} following the atmospheric CO_2 increase, we added 1.8 µatm to 280 µatm for the Canada Basin for each subsequent year. The initial Alk was calculated from the SSS using the relationship described above, and the initial DIC was determined by the initial Alk and p_{CO_2} in the CO2SYS program.

NCP setting. The NCPs in the Chukchi Shelf and Canada Basin reported in previous studies are summarized in Supplementary Table 3. As the primary production is patchy and widely variable on the shelf on the interannual time scale, it is difficult to set values for each month or find the best value that works well for the entire shelf. We conducted sensitivity tests by using different NCP rates for the simulation and found that a slight change (within the range of 5–30 mmol C m^{-2} d^{-1}) in the value of NCP for Chukchi Shelf would affect only the lowest values of p_{CO_2} during the summer, but would not significantly change the long-term trends (Supplementary Fig. 3). Thus, to keep the model simple, we chose a value of 10 mmol C m^{-2} d^{-1} for the simulation, which generally reflected the observed p_{CO_2} trend on the Chukchi Shelf. To investigate the impact of recent enhanced NCP on the Chukchi Shelf[8], we applied an increase of NCP by 30% since 2007 to compare with the constant NCP scenarios (Fig. 4a,b).

The NCP in the Canada Basin was much lower than that in the Chukchi Shelf (Supplementary Table 3), and no significant change trend was observed[48]. We therefore set a constantly low NCP of 1 mmol C m^{-2} d^{-1} for the basin surface water for the simulation.

Simulation step. The time interval of the simulation step is 1 d. For each simulation step, the sea surface p_{CO_2} was calculated using the CO2SYS program with Alk and DIC. The daily change in DIC inventory in the surface mixed layer was calculated as follows:

$$\Delta DIC_t = (FCO_2 + NCP)/MLD + \Delta DIC_{(diluted)} \quad (16)$$

$$DIC_{t+1} = DIC_t + \Delta DIC_t \quad (17)$$

where F_{CO_2} and $\Delta DIC_{(diluted)}$ indicate the changes in DIC inventory induced by CO_2 air–sea flux and meltwater dilution, respectively.

The air–sea CO_2 flux (F_{CO_2}) was calculated following:

$$F_{CO_2} = K_s \times k_{CO_2} \times \Delta p_{CO_2} \quad (18)$$

where K_s and k_{CO_2} are the solubility of CO_2 and the CO_2 gas transfer velocity, respectively. The solubility of CO_2 was calculated from the daily average SST (ref. [49]) and estimated salinity. The value of k_{CO_2} is calculated with the monthly second moment of wind speed at 10 m in height, $<U_{10}^2>$, following the equation described in ref. [50]:

$$k_{CO_2} = -0.251 \times <U_{10}^2> \times (Sc/660)^{-0.5} \times (1 - ice\%/100) \quad (19)$$

where Sc indicates the Schmidt number. The four-times daily surface (10 m) wind speed was obtained from the NCEP-DOE Reanalysis 2 data (https://www.esrl.noaa.gov/psd/data/gridded/data.ncep.reanalysis2.html). For each day, the six-hourly wind speed squared was calculated and then averaged into a daily mean and subsequently into the monthly mean value. The value of k_{CO_2} was adjusted according to the ice%. The daily ice% was obtained from the Scanning Multichannel Microwave Radiometer on the Nimbus-7 satellite and from the Special Sensor Microwave/Imager sensors on the Defense Meteorological Satellite Program's -F8, -F11, and -F13 satellites with a resolution of 25 km × 25 km (ref. [51]).

The monthly averaged atmospheric CO_2 concentrations in dry air (xCO_2) were downloaded from NOAA's Earth System Research Laboratory at Point Barrow, Alaska (https://www.esrl.noaa.gov/gmd/dv/data/index.php?parameter_name=Carbon%2BDioxide&frequency=Monthly%2BAverages&site=BRW), and corrected to p_{CO_2} for water vapour pressure using the following equation:

$$p^{air}_{CO_2(monthly)} = xCO_{2(monthly)} \times (Psl_{(monthly)} - Pw_{(monthly)}) \quad (20)$$

where Psl and Pw are the sea level and water vapour pressures, respectively. The monthly Psl was obtained from the satellite reanalysis product (NCEP-DOE Reanalysis 2, https://www.esrl.noaa.gov/psd/data/gridded/data.ncep.reanalysis2.html) with a resolution of 2.5° × 2.5°. The monthly Pw was calculated from Psl and SST (ref. [52]).

With monthly $p^{air}_{CO_2}$, the difference between atmospheric and sea surface p_{CO_2} (Δp_{CO_2}) was calculated. The long-term trends of Δp_{CO_2} in four subregions were examined with the monthly Δp_{CO_2} (Extended Data Fig. 4).

We simplified the ice melt dilution process in the simulation by assuming that the ratio of Alk to DIC in the ice nearly equals that in the surface seawater; thus, the change in DIC by dilution could be estimated as follows:

$$\Delta DIC_{t(diluted)} = (Alk_{t+1} - Alk_t)/Alk_t \times DIC_t \quad (21)$$

With the new DIC and Alk for the next simulation step, a new p_{CO_2} was calculated, and this simulation process repeats until the last day.

The model simulation settings and the sources of data used in the model are summarized in Supplementary Table 4.

Reporting Summary. Further information on research design is available in the Nature Research Reporting Summary linked to this article.

Data availability

Source Data for Extended Data Fig. 5 are provided with the paper. All the data are archived in publicly accessible databases, and the data sources are listed in the main text, Methods and Supplementary Information. The assembled p_{CO_2} dataset used in this study is available in the Supplementary Information.

Code availability

The code used for p_{CO_2} simulations is available in the Supplementary Information. R programming software was used to generate all the results. The saved simulation results are available on request from the corresponding author.

References

38. Bakker et al. A multi-decade record of high quality data in version 3 of the Surface Ocean CO_2 Atlas (SOCAT). *Earth Syst. Sci. Data* **8**, 383–413 (2016).
39. Takahashi, T., Sutherland, S. & Kozyr, A. *Global Ocean Surface Water Partial Pressure of CO_2 Database: Measurements Performed During 1957–2017 (LDEO Database Version 2017) (NCEI Accession 0160492)* (National Oceanic and Atmospheric Administration, Department of Commerce, accessed 28 August, 2018).
40. Pierrot, D. et al. Recommendations for autonomous underway measuring systems and data-reduction routines. *Deep Sea Res. 2* **56**, 512–522 (2009).
41. Pierrot, D., Lewis, E. & Wallace, D. W. R. MS Excel program developed for CO_2 system calculations. ORNL/CDIAC-105a. v2.1(Carbon Dioxide Information Analysis Center, Oak Ridge National Laboratory, U.S. Department of Energy, 2006).
42. Lueker, T. J., Dickson, A. G. & Keeling, C. D. Ocean p_{CO_2} calculated from dissolved inorganic carbon, alkalinity, and equations for K1 and K2: validation based on laboratory measurements of CO_2 in gas and seawater at equilibrium. *Mar. Chem.* **70**, 105–119 (2000).
43. Woosley, R. J., Millero, F. J. & Takahashi, T. Internal consistency of the inorganic carbon system in the Arctic Ocean. *Limnol. Oceanogr. Methods* **15**, 887–896 (2017).
44. Sarmiento, J. L., & Gruber, N. Ocean Biogeochemical Dynamics (Princeton Univ. Press, 2006).
45. Olsen, A. et al. GLODAPv2.2019—an update of GLODAPv2. *Earth Syst. Sci. Data* **11**, 1437–1461 (2019).
46. Friis, K., Körtzinger, A. & Wallace, D. W. The salinity normalization of marine inorganic carbon chemistry data. *Geophys. Res. Lett.* **30**, 1085 (2003).
47. Rysgaard, S., Glud, R. N., Sejr, M. K., Bendtsen, J. & Christensen, P. B. Inorganic carbon transport during sea ice growth and decay: a carbon pump in polar seas. *J. Geophys. Res. Oceans* **112**, C03016 (2007).
48. Ji, B. Y. et al. Variations in rates of biological production in the Beaufort Gyre as the Arctic changes: rates from 2011 to 2016. *J. Geophys. Res. Oceans* **124**, 3628–3644 (2019).
49. Weiss, R. Carbon dioxide in water and seawater: the solubility of a non-ideal gas. *Mar. Chem.* **2**, 203–215 (1974).
50. Wanninkhof, R. Relationship between wind speed and gas exchange over the ocean revisited. *Limnol. Oceanogr. Methods* **12**, 351–362 (2014).
51. Comiso, J. C. Bootstrap Sea Ice Concentrations from Nimbus-7 SMMR and DMSP SSM/I-SSMIS v.2 (NASA National Snow and Ice Data Center Distributed Active Archive Center, accessed 21 August, 2018).
52. Buck, A. L. New equations for computing vapor pressure and enhancement factor. *J. Appl. Meteorol.* **20**, 1527–1532 (1981).
53. Fetterer, F., Knowles, K., Meier, W. N., Savoie, M. & Windnagel, A. K. Sea Ice Index v.3 (National Snow and Ice Data Center, accessed 10 November, 2018).

Acknowledgements

We thank the contributors to the SOCAT v.5, LDEO, CHINARE, JAMSTEC, USGS, NSF Arctic Data Center and CDIAC datasets, as well as the research vessels and crews for collecting the data used in this study. We thank H. Wang for helpful discussion. This work was supported by the US NSF (grant nos ARC-0909330, PLR-1304337, OPP-1926158, PLR-1220032, PLR-1504410, OPP−1735862 and PLR-1723308), NOAA (grant nos NA09OAR4310078, NA150OAR4320064 and NA10NOS4000073),

Interdisciplinary Research for Arctic Coastal Environments funded by US Deparment of Energy (DOE InteRFACE project), the National Natural Science Foundation of China (grant nos 41806222, 41630969, 41230529, 41476172 and 41706211), the Chinese Projects for Investigations and Assessments of the Arctic and Antarctic (grant no. CHINARE2017-2020), the National Key Research and Development Program of China (grant no. 2019YFA0607003), the Scientific Research Foundation of Third Institute of Oceanography, SOA (grant nos 2018005 and 2017029), the Bilateral Cooperation of Maritime Affairs (grant no. 2200207), Fujian science and technology innovation leader project 2016, and the Arctic Challenge for Sustainability (ArCS) Project funded by the Ministry of Education, Culture, Sports, Science and Technology of Japan (MEXT).

Author contributions

L.C. and W-J.C. organized the collaborative research on the Arctic Ocean Carbon Cycle and Acidification Project via CHINARE cruises. Z.O., W-J.C. and T.T. prepared the paper. Z.O., D.Q., B.C., Z.G. and H.S. executed the fieldwork. Z.O., W.Z., D.Q. and B.C. analysed the data. Z.O. did the model simulations. T.T., M.D.D., A.M., S.N., M.J. and L.L.R. contributed the data and materials. All authors contributed to the discussion and writing.

Competing interests

The authors declare no competing interests.

Additional information

Extended data is available for this paper at https://doi.org/10.1038/s41558-020-0784-2.

Supplementary information is available for this paper at https://doi.org/10.1038/s41558-020-0784-2.

Correspondence and requests for materials should be addressed to W.-J.C.

Reprints and permissions information is available at www.nature.com/reprints.

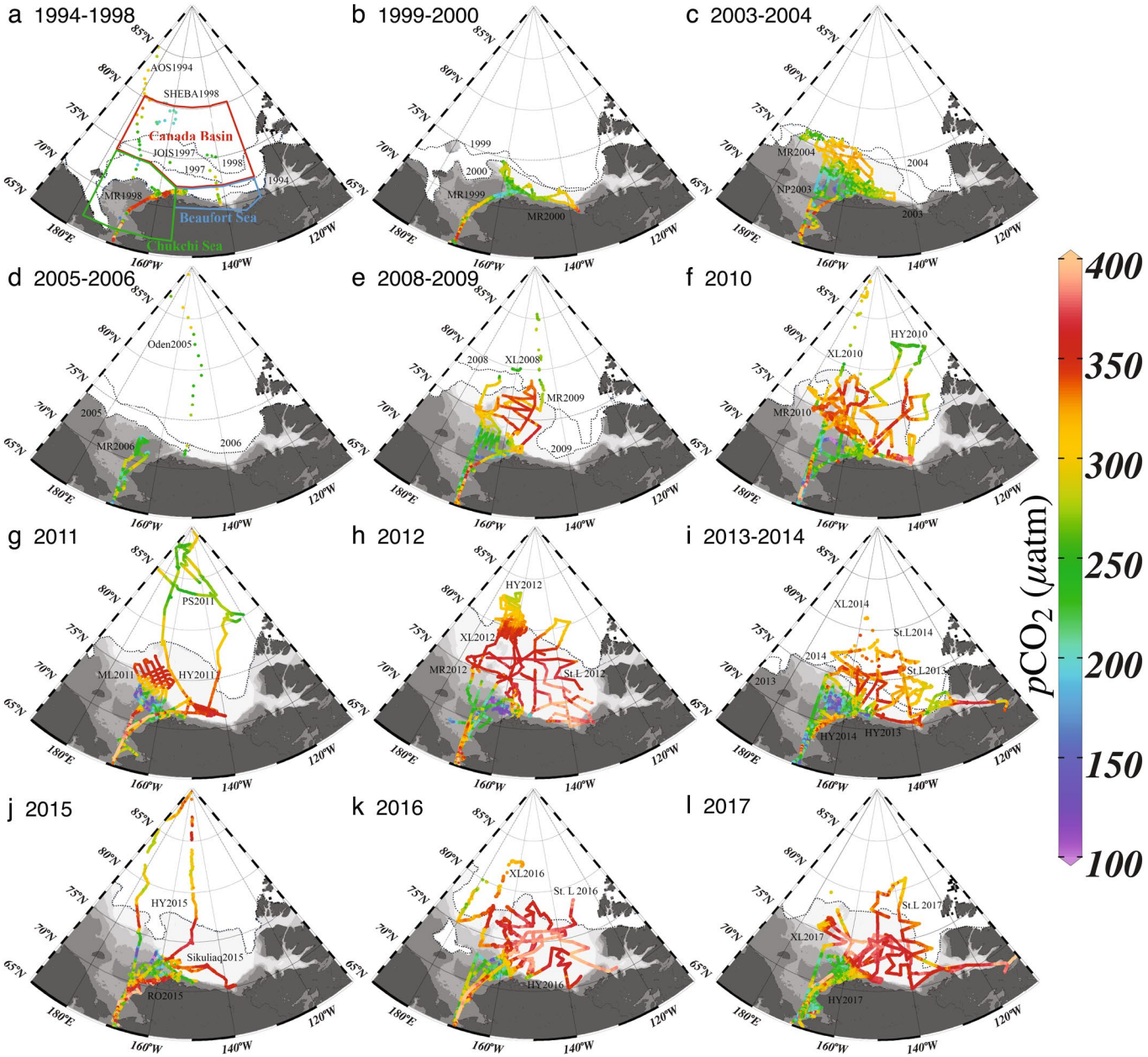

Extended Data Fig. 1 | The distribution of sea surface pCO_2 at in situ temperature in the western Arctic Ocean. All pCO_2 data was measured by underway pCO_2 systems except datasets in AOS1994, JOIS 1997, SHEBA 1998 and ODEN 2005 cruises, which were calculated from discrete samples. MR, NP, ODEN, XL, ML, PS, HY, RO, St. L, and Sikuliaq stand for the Research Vessel Mirai, Nathaniel B. Palmer, ODEN, Xuelong, Marcus G. Langseth, Polarstern, Healy, Ronald H. Brown, Louis S. St-Laurent, and Sikuliaq, respectively. A list of cruise information is provided in Supplementary Table 1. The white areas with dashed lines indicate monthly sea ice extent (ice concentration >15%) in September, which has the minimal sea ice extent (Nation Snow and Ice Data Center, http://nsidc.org/data/seaice_index/)[53].

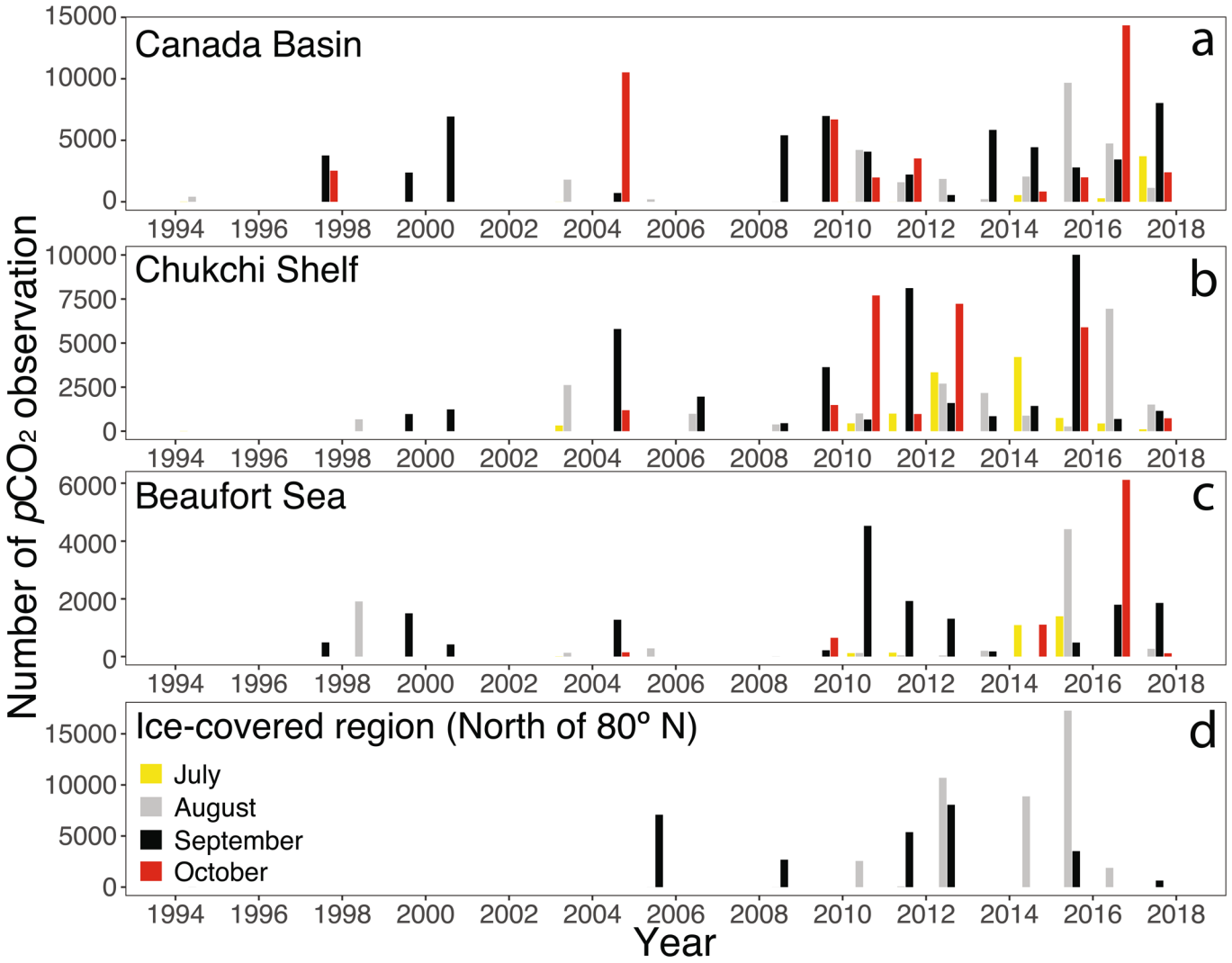

Extended Data Fig. 2 | Monthly time series of the number of sea surface pCO_2 measurements in the western Arctic Ocean. (**a**) Canada Basin, (**b**) Chukchi Shelf, (**c**) Beaufort Sea, (**d**) Ice-covered region (north of 80ºN). For a given subregion, the number of pCO_2 observations for each month could vary greatly among years depending on the number and timing of cruises, and the sea-ice conditions in a particular year. The number of pCO_2 values substantially increased after 2007.

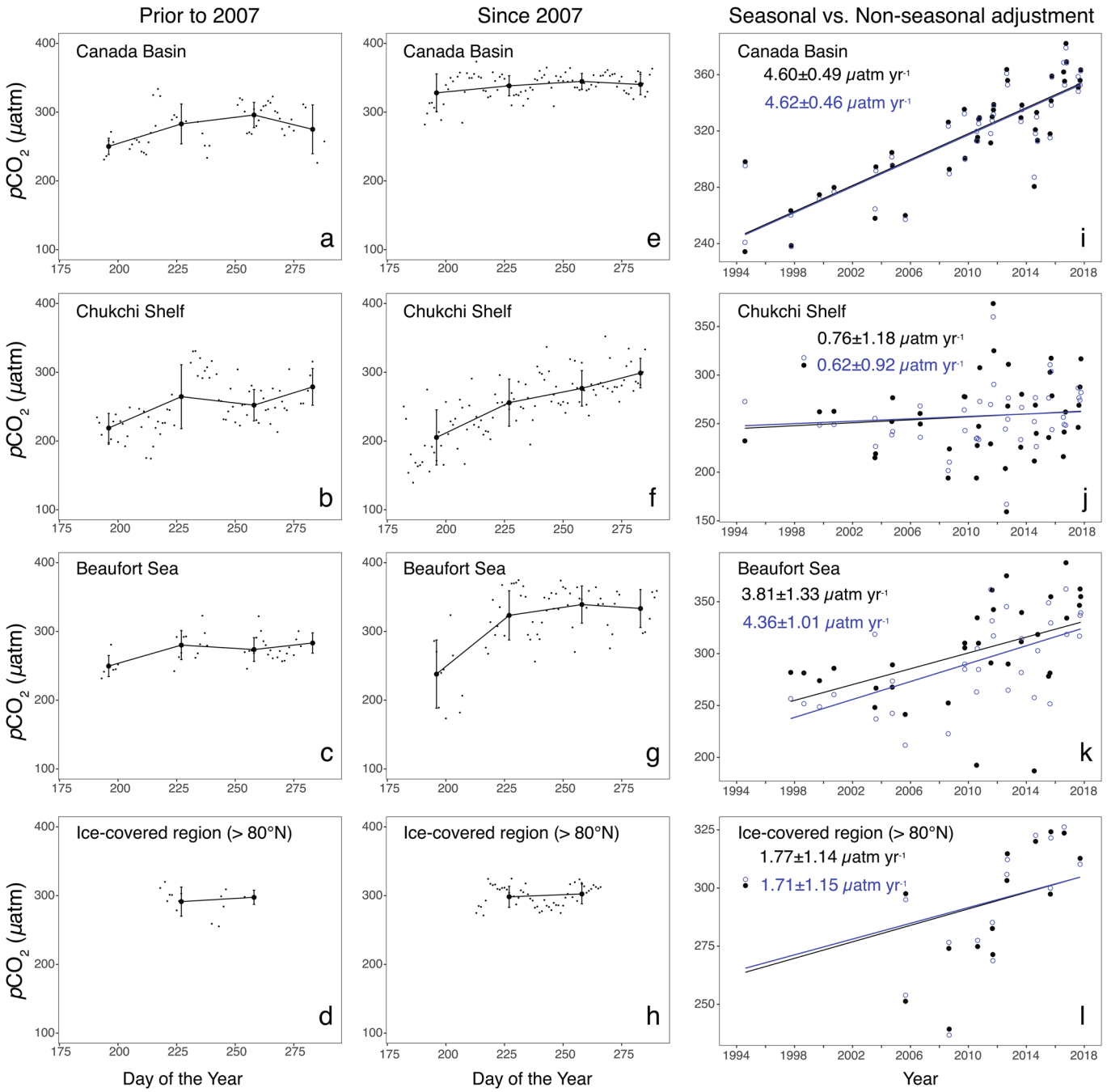

Extended Data Fig. 3 | The changes in the seasonality of pCO_2 and deseasonalized long-term trends. We examined the seasonal variation of pCO_2 by binning gridded (0.1° latitude × 0.25° longitude) values into Julian-Day for two periods: years prior to 2007 (**a**–**d**) and 2007 to 2017 (**e**-**h**). We deseasonalized data to calculate monthly means of pCO_2 following the method described in ref. [16]. Briefly, we detrended pCO_2 data first and then adjusted the monthly means by adding or subducting the anomaly with respect to the long-term summer mean (averaged over 1994-2017), assuming that the seasonal variations remained unchanged over years. The black and blue dots represent non- and seasonal adjusted monthly means of pCO_2, respectively (**i**–**l**). The rates of change with standard error are noted.

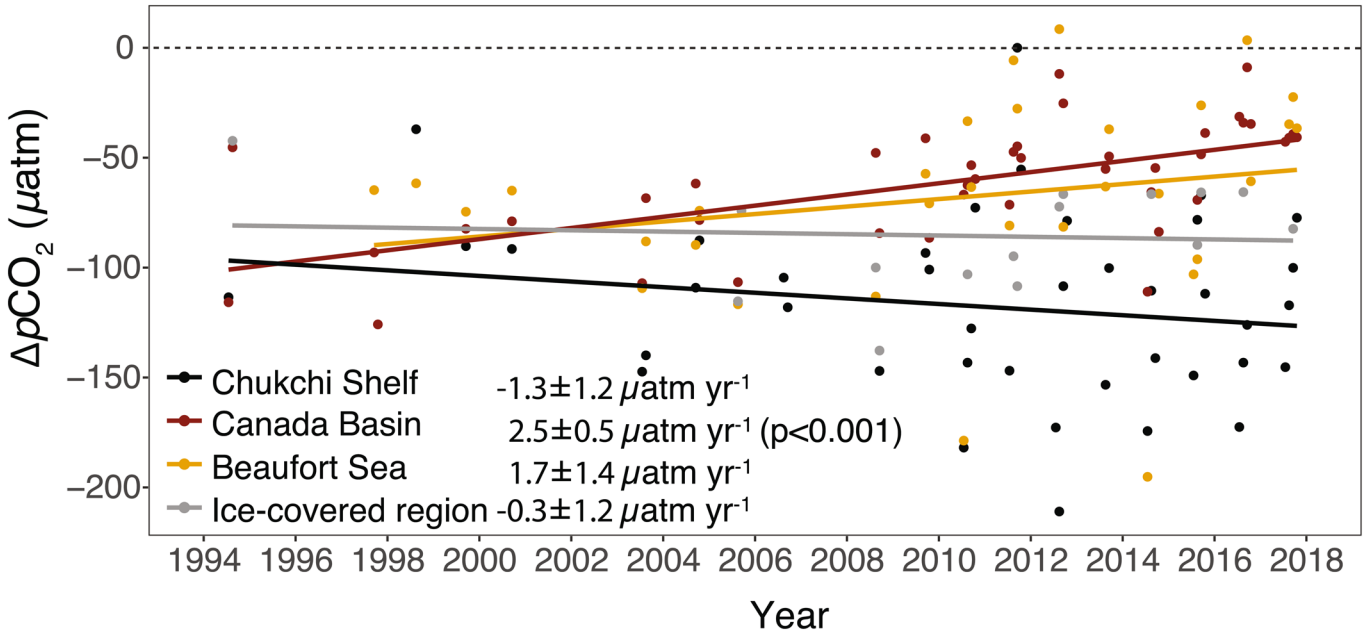

Extended Data Fig. 4 | The trends of CO_2 air-sea gradient (ΔpCO_2). The summer ΔpCO_2 vary in the Chukchi Shelf, the Canada Basin, the Beaufort Sea and ice-covered region over the period of 1994 to 2017. The rates of change of ΔpCO_2 were computed with monthly mean values (positive rates indicate decrease in ΔpCO_2, while negative rates indicate increase in ΔpCO_2). The dashed line indicates a complete air-sea gas equilibrium. ANOVA was performed for all regressions. Only ΔpCO_2 in the Canada Basin shows a significant trend.

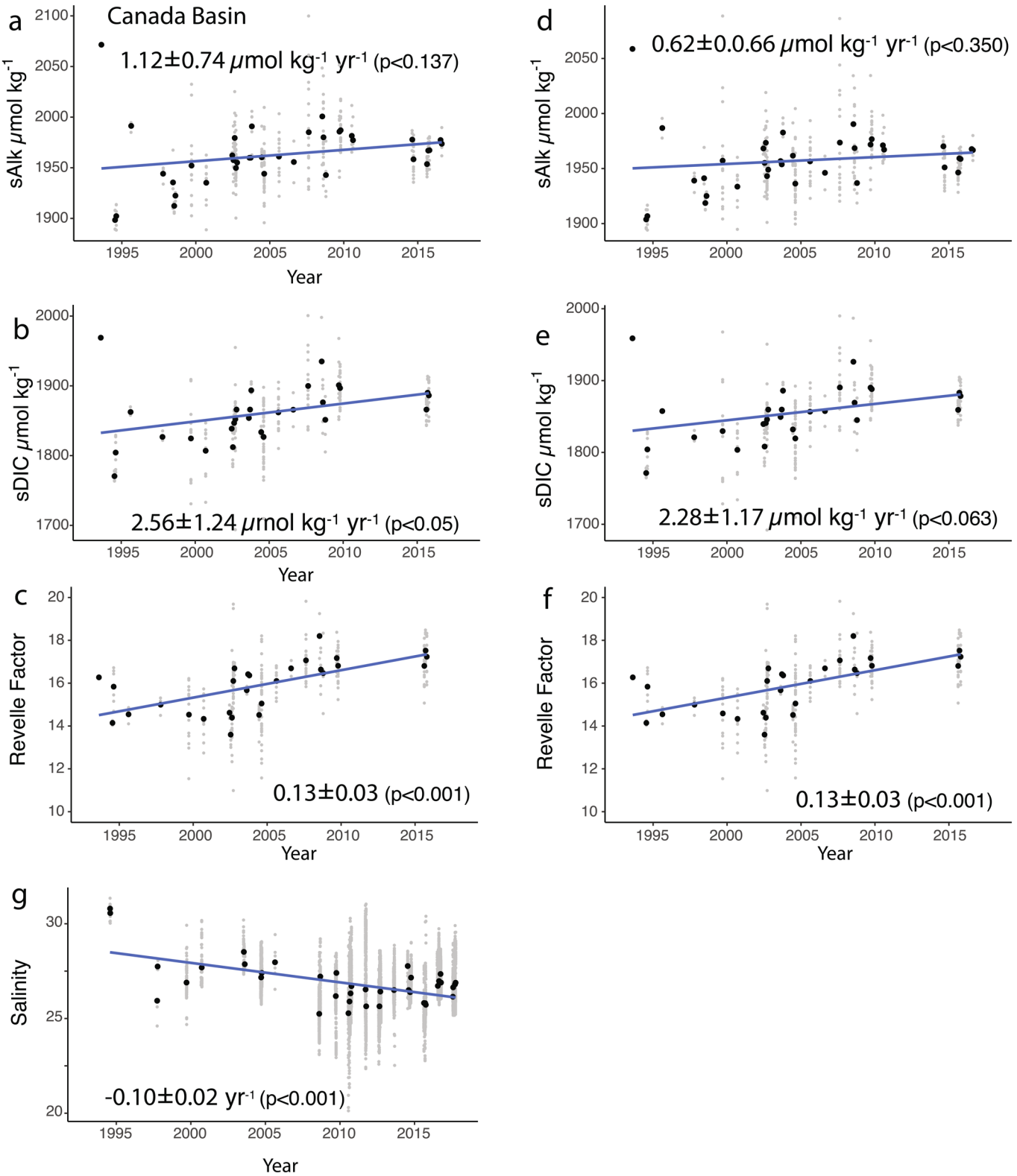

Extended Data Fig. 5 | The long-term trends of sea surface sAlk, sDIC, Salinity, and Revelle Factor in the Canada Basin. The discrete samples of sea surface (depth < 20 m) Alk and DIC were obtained from the Global Data Analysis Project version 2 database[38] (grey dots). We calculated salinity normalized DIC (sDIC = DIC×S_0/SSS) and Alk (sAlk = Alk×S_0/SSS) and then averaged the data to calculate monthly means (black dots) for the linear regressions (**a** and **b**). The S_0 is the reference salinity, i.e. the long-term mean of SSS. We also conducted a non-zero endmember salinity normalization[39] for DIC and Alk (**d** and **e**; see Methods). The corresponding Revelle Factor was calculated in the CO2SYS program (**c** and **f**). The underway measurement of salinity was used for examining the long-term trend (**g**). We tested whether the slope significantly different from 0 by ANOVA. The rates of change with standard error are shown.

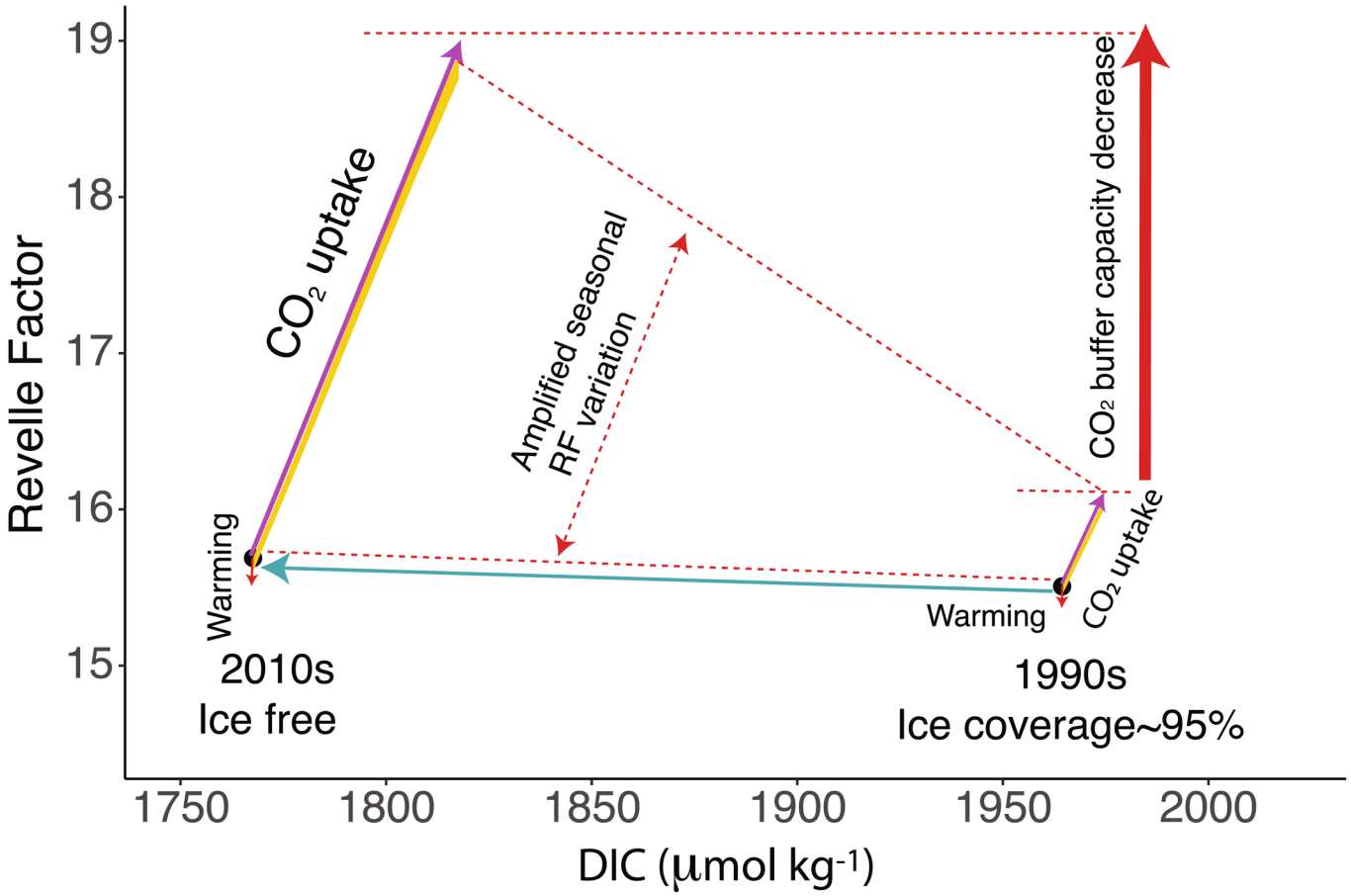

Extended Data Fig. 6 | Sea ice-loss amplifying the decrease in surface water Revelle Factor (RF) in the Canada Basin. Black dots represent the initial condition for RF and DIC at -1.6 °C. The arrows indicate the processes of warming (red), CO_2 uptake from the atmosphere (purple), dilution by ice meltwater (cyan). Sea ice reduction from 95% to ice-free is accompanied by a salinity decrease of 3.5 (Supplementary Table 4). The yellow shaded areas indicate the possible seasonal variations of RF, which are amplified by the synergistic effect of ice melt, warming and CO_2 uptake. To estimate the change of RF, we allowed 2 °C and 3 °C warming, and 10 and 50 μmol kg^{-1} DIC perturbations due to air-sea CO_2 exchange in 1990s and 2010s, respectively, which are consistent with the long-term warming rate of 0.5 °C per decade[34] and the estimated increase in sDIC by 2.3-2.6 µmol kg^{-1} per year (Table 1 and Fig. 4d). Note that higher RF indicates lower acid-base buffer capacity.

nature research

Corresponding author(s): Wei-Jun Cai

Last updated by author(s): Apr 6, 2020

Reporting Summary

Nature Research wishes to improve the reproducibility of the work that we publish. This form provides structure for consistency and transparency in reporting. For further information on Nature Research policies, see Authors & Referees and the Editorial Policy Checklist.

Statistics

For all statistical analyses, confirm that the following items are present in the figure legend, table legend, main text, or Methods section.

n/a	Confirmed	
☒	☐	The exact sample size (*n*) for each experimental group/condition, given as a discrete number and unit of measurement
☒	☐	A statement on whether measurements were taken from distinct samples or whether the same sample was measured repeatedly
☒	☐	The statistical test(s) used AND whether they are one- or two-sided *Only common tests should be described solely by name; describe more complex techniques in the Methods section.*
☒	☐	A description of all covariates tested
☒	☐	A description of any assumptions or corrections, such as tests of normality and adjustment for multiple comparisons
☐	☒	A full description of the statistical parameters including central tendency (e.g. means) or other basic estimates (e.g. regression coefficient) AND variation (e.g. standard deviation) or associated estimates of uncertainty (e.g. confidence intervals)
☐	☒	For null hypothesis testing, the test statistic (e.g. *F*, *t*, *r*) with confidence intervals, effect sizes, degrees of freedom and *P* value noted *Give P values as exact values whenever suitable.*
☒	☐	For Bayesian analysis, information on the choice of priors and Markov chain Monte Carlo settings
☒	☐	For hierarchical and complex designs, identification of the appropriate level for tests and full reporting of outcomes
☒	☐	Estimates of effect sizes (e.g. Cohen's *d*, Pearson's *r*), indicating how they were calculated

Our web collection on statistics for biologists contains articles on many of the points above.

Software and code

Policy information about availability of computer code

Data collection	The code used for pCO2 simulations is available in supplementary material. The software used to generate all the results is R programming language.
Data analysis	The code used for pCO2 simulations is available in supplementary material. The software used to generate all the results is R programming language.

For manuscripts utilizing custom algorithms or software that are central to the research but not yet described in published literature, software must be made available to editors/reviewers. We strongly encourage code deposition in a community repository (e.g. GitHub). See the Nature Research guidelines for submitting code & software for further information.

Data

Policy information about availability of data

All manuscripts must include a data availability statement. This statement should provide the following information, where applicable:

- Accession codes, unique identifiers, or web links for publicly available datasets
- A list of figures that have associated raw data
- A description of any restrictions on data availability

All data are archived in public data centers and the sources are listed in the main text and methods. The assembled pCO2 dataset using in this study is available in supplementary material.

Field-specific reporting

Please select the one below that is the best fit for your research. If you are not sure, read the appropriate sections before making your selection.

☐ Life sciences ☐ Behavioural & social sciences ☒ Ecological, evolutionary & environmental sciences

For a reference copy of the document with all sections, see nature.com/documents/nr-reporting-summary-flat.pdf

Ecological, evolutionary & environmental sciences study design

All studies must disclose on these points even when the disclosure is negative.

Study description	We report changes of summer pCO2 from 1994-2017 in the western Arctic Ocean by synthesizing all available historical pCO2 data and examining the seasonal and long-term variations.
Research sample	Most of the data used in this study is underway measured sea surface pCO2. A few pCO2 in early years was calculate from discrete samples of DIC and TA.
Sampling strategy	The sea surface pCO2 were collected along the pre-determined transect lines.
Data collection	The sea surface underway pCO2 was measured with a non-dispersive infrared analyzer of CO2 in the equilibrated headspace gas by an underway CO2 system (General Oceanic, USA) during 2008, 2010, 2012, 2014, 2016 and 2017 CHINARE (Chinese Arctic Research Expedition) cruises. Other pCO2 data are obtained from multiple international databases.
Timing and spatial scale	pCO2 measured in summer months (July 1 to October 15) from 1994 to 2017. Spatial scale is the western Arctic Ocean, including the Chukchi Shelf, Beaufort Sea, and Canada Basin.
Data exclusions	We excluded the data outside the study area assigned in the Fig. 1.
Reproducibility	Data can be re-analyzed and uncertainties can be re-assessed.
Randomization	n/a
Blinding	n/a

Did the study involve field work? ☒ Yes ☐ No

Field work, collection and transport

Field conditions	Most of the field work are ship-based.
Location	The western Arctic Ocean, including the Chukchi Shelf, Beaufort Sea, and Canada Basin.
Access and import/export	n/a
Disturbance	n/a

Reporting for specific materials, systems and methods

We require information from authors about some types of materials, experimental systems and methods used in many studies. Here, indicate whether each material, system or method listed is relevant to your study. If you are not sure if a list item applies to your research, read the appropriate section before selecting a response.

Materials & experimental systems

n/a	Involved in the study
☒	☐ Antibodies
☒	☐ Eukaryotic cell lines
☒	☐ Palaeontology
☒	☐ Animals and other organisms
☒	☐ Human research participants
☒	☐ Clinical data

Methods

n/a	Involved in the study
☒	☐ ChIP-seq
☒	☐ Flow cytometry
☒	☐ MRI-based neuroimaging